Modeling and Estimation of the Volume of Interaction of an Electrostatic Force Microscope Probe with a Dielectric Sample

by

Everet Anema

A Thesis submitted to the Faculty of Graduate Studies of

The University of Manitoba

in partial fulfilment of the requirements of the degree of

MASTER OF SCIENCE

Department of Electrical and Computer Engineering

University of Manitoba

Winnipeg

Copyright © 2011 by Everet Anema

Abstract

This thesis seeks to characterize the size of the interaction volume in a sample subject to electric force microscope (EFM) probing. It discusses the historical relevance of the EFM and the experimental method used. It then discusses the modeling of the fields surrounding the grating sample with the equivalent charge model (ECM) where a tip or other rotationally symmetric conducting element is replaced by a series of point charges on the vertical axis that mimic the original fields. The results of the model were then compared to the experimental data as well as a model simulated using *COMSOL*, a finite element analysis package. The electrostatic model was found to have good agreement with the simulated and experimental results and was then used to estimate the volume of interaction and the lateral resolution of this technique. The volume of interaction was estimated at 6000 μm^3 and the lateral resolution was estimated at 10 μm.

Acknowledgments

I would like to thank my supervisor, Dr. Derek Oliver for proposing this topic and allowing me the opportunity to take my studies further. I am very grateful for his straight-shooting, to the point method of dealing with me – his door was always open to my countless enquiries. This thesis would not have been possible without all of his guidance (and patience) along the way. Thank you.

I would also like to thank Iman Yahyaie for his patience in dealing with my many problems with the SPM rig. His extreme patience and steady hands had an aptitude for dealing all the equipment that I broke. Thank you.

I would also like to thank Dominic Schaub for his aid in debugging my mathematical models. His help and guidance was an excellent resource to have sitting behind me in the office. I could comfortably bounce ideas off him without a thought of how I was distracting him from his work. Thank you.

Electronic Materials

This CDROM contains *MATLAB* scripts and *COMSOL* models used in the implementation and verification of the models described in this thesis. The *MATLAB* scripts require *MATLAB* version R2009B or greater and the *COMSOL* models were created using *COMSOL* V3.5A.

Table of Contents

Abstract ii
Acknowledgments iii
Electronic Materials iv
Table of Contents v
List of Tables vi
List of Figures vi

1 Introduction 1
1.1 Evolution of Microscopy 1
1.2 Overview 8
2 Experimental Theory and Setup 11
2.1 EFM Background 11
2.2 Heterodyne Electrostatic Imaging 12
2.3 Experimental Setup 15
3 Electrostatic Modelling of EFM Setup 22
3.1 Introduction 22
3.2 Field due to a Single Point Charge 25
3.3 Equivalent Charge Model 30
3.4 Post Processing 35
4 Results and Discussion 38
4.1 Experimental Data Analysis 38
4.1.1 Interpreting the Data 38
4.1.2 Data Collection 42
4.2 Analytical Data Analysis 47
4.2.1 Lateral Resolution 52
4.2.2 Depth versus Relative Permittivity 55
5 Numerical Electrostatic Modelling 57
5.1 Introduction to Finite Element Analysis and *COMSOL* 57
5.2 Verification of Analytic Model 58
5.3 Determination of Ratio Inversion 64
5.4 Scan Line over SiO_2 Step 68
6 Conclusions 75
6.1 Future Work 77
7 References 79

List of Tables

Table 5.1: Fit parameters for the *COMSOL* simulations and experimental data. **72**

List of Figures

Figure 1.1: STM image of an atomically resolved chiral nanotube [8] **4**
Figure 2.1: Experimental setup. The cantilever voltage is driven by an applied amplitude modulated signal. The change in position of the cantilever is detected using a beam bounce system and sent to a lock-in amplifier to be analyzed and recorded by a computer. **13**
Figure 2.2: Experimental Apparatus consists of a personal computer (A) connected to a Veeco EnviroScope controller (B) and a NanoScope IIIa AFM controller (C) connected to a breakout box (D). The controllers operate the EnviroScope (E) which is isolated on an air table (F). **15**
Figure 2.3: Beam bounce system used to detect horizontal and vertical deflection using a four quadrant split photodetector. **17**
Figure 2.4: Quality factor of the cantilever versus the air pressure in the vacuum chamber. The error reflects the size of the frequency bins as the data was captured 50 times and averaged by the spectrum analyzer. **19**
Figure 3.1: TGZ series sample grating used to validate the model. A) Tip centred above SiO2 grating. B) Tip centred above Si substrate **22**
Figure 3.2: Voltage found using the ECM. Point charges and test points are marked. **25**
Figure 3.3: A point charge Q is located at the origin with two dielectric boundaries at z=a and z=b. This forms three distinct regions, region 1, 2 & 3. ..... **26**
Figure 3.4: Two equal but opposite point charges are mirrored about the plane z=0. The dielectric configuration is also mirrored about this plane. **28**
Figure 3.5: The voltage due to a single point charge about three dielectric regions above a ground plane. From top to bottom, ε_{r1}=1, ε_{r2}=12 & ε_{r3}=4. ..... **29**
Figure 3.6: Tip geometry illustrating the switch over point between the conical and spherical distributions **33**
Figure 3.7: RMS error of the equivalent charge model varies with the number of point charges used to model the tip. **34**
Figure 3.8: RMS error of the equivalent charge model varies with the number of test points used. This plot was generated with N_c=40. ..... **35**
Figure 3.9: Plot of Force versus Depth for the equation of (3.19) **37**
Figure 4.1: A force plot created by plotting the displacement of the piezo in the z direction versus the voltage representing vertical displacement of the cantilever. This plot was created by engaging the tip into the aluminum sample holder. **39**
Figure 4.2: Cumulative sum of a scaled displacement spectrum. This data was collected using the NSC18 cantilever at room temperature an pressure. **41**
Figure 4.3: A typical scan of the TGZ-02 sample grating taken at a lift height of 300 nm and an applied voltage of 3V. The image on the left is height data and the image on the right is the electrostatic response of the tip. **44**

Figure 4.4: Amplitude of vibration of the cantilever (which is proportional to force) when above silicon versus cantilever lift height for applied voltage of 1 to 4 Volts. **45**
Figure 4.5: Amplitude of vibration of the cantilever when above silicon dioxide versus cantilever lift height for applied voltage of 1 to 4 Volts. **45**
Figure 4.6: The ratio response for several voltages versus the lift height of the cantilever. **47**
Figure 4.7: This is the subset of the data in Figure 4.6 representing the far response asymptotically approaching a ratio of one. The dashed line represents an average approach to unity. **47**
Figure 4.8: Force above Si calculated on the tip versus cantilever lift height for applied voltage of 1 to 4 Volts. **48**
Figure 4.9: Force above SiO_2 calculated on the tip versus cantilever lift height for applied voltage of 1 to 4 Volts. **49**
Figure 4.10: The ratio response calculated as a function of lift height **49**
Figure 4.11: Total force (%) acting on the cantilever found by calculating the Maxwell stress tensor over a volume defined by the depth of its deepest point. **51**
Figure 4.12: Depth of interaction volume versus lift height for a tip above SiO_2 and Si. **51**
Figure 4.13: Interaction volume versus lift height for a tip above SiO_2 and Si. 51
Figure 4.14: Response function of the NSC-18 cantilever tip at a lift height of 300 nm **55**
Figure 4.15: Predicted resolution versus lift height **55**
Figure 4.16: Depth of interaction plotted against the relative permittivity of an infinite dielectric sheet 430 μm thick resting on a ground plane with a tip-sample separation of 300 nm. **56**
Figure 5.1: Left: The schematic representation of the analytical model in COMSOL; Middle: The mesh used to solve this model; Right: The voltage plot of the solution. **60**
Figure 5.2: COMSOL solution focused on the voltage near the tip. The vertical line represents the region where the comparison was made. **61**
Figure 5.3: Comparison of COMSOL results to the analytical model along the vertical line crossing the SiO_2 layer. **62**
Figure 5.4: Comparison of COMSOL results to the analytical model at the test points along the surface of the tip. **62**
Figure 5.5: Left: Schematic depiction of the substitution of point charges with a triangular tip shape. Middle: The mesh used to solve this model. Right: The voltage plot of the solution. **63**
Figure 5.6: Left: Schematic depiction of the tip with cantilever. Middle: The mesh used to solve the model. Right: The voltage plot of the solution. **65**
Figure 5.7: The four positions of the tip used to determine the nature of the ratio inversion. **66**
Figure 5.8: Far response and near response with and without the cantilever included in the model. **67**
Figure 5.9: A) Schematic view of the tip over the sample surface in the COMSOL simulation environment. B) Enlarged view of the tip-sample region as the tip is scanned from left to right. **69**
Figure 5.10: Graphical representation of the model fitted to the data sets. The parameters include a, b, x_0 and τ. **70**
Figure 5.11: The force calculated by COMSOL acting on the tip versus the offset from

the step edge forms the sparse data while the experimental amplitude of vibration, which is proportional to force acting on the tip versus the offset from the step edge forms the solid line. The COMSOL data is represented by the left vertical axis and the experimental data is represented by the right vertical axis. The relation to the surface profile is shown on the lower plot for both COMSOL and the experimental data. **71**
Figure 5.12: The Logistic function fit to the experimental data and the COMSOL simulated data. **72**
Figure 5.13: Depth of interaction plotted against the offset of the tip from the SiO_2 step edge. The solid line represents the data fitted to (5.4) and the dashed line represents the surface profile. **74**
Figure 5.14: Volume of interaction plotted against the offset of the tip from the SiO_2 step edge. The solid line represents the data fitted to (5.4) and the dashed line represents the surface profile. **74**

1 Introduction

1.1 Evolution of Microscopy

The optical microscope was first developed during the European Renaissance [1]. The magnification factor of the first optical microscopes was extremely poor by today's standards but provided a basis for improvement and innovation. In 1873 Ernst Abbe was credited for discovering the diffraction limit of optical microscopes while employed by Carl Zeiss [2]. This limit implies that there is a maximum resolution that can be achieved by traditional optical microscopes in the range of 50 to 100 nm under optimal conditions [3].

In 1928, E. H. Synge published a new idea that formed the basis for the modern scanning probe microscopes [3]. In abstract terms, Synge described a method to obtain an image at resolutions much smaller than the wavelength of visible light (Synge suggested 10 nm) using what is now known as near-field scanning optical microscopy (NSOM). The method proposed raster scanning a 10 nm aperture in a section of silver foil held in close proximity to the surface of the sample, which would be intensely illuminated from behind. An image of the sample could then be collected pixel by pixel and displayed as an image using another light source such as a CRT display. Four technical difficulties were cited, most interestingly how to position the aperture with respect to the sample under study. The first solution involved mechanical actuators that positioned the aperture by means of screw adjustments, such as the micromanipulators used on modern microscopes. In 1932, Synge published an update to his previous publication in which he

suggested that the mechanical actuators could be replaced by three piezoelectric quartz crystals (one for each Cartesian axis) so that the position of the aperture would be controlled electronically by applying a voltage across each crystal [4]. This approach would provide a fast, reliable means of positioning and raster scanning a probe across a surface, as employed by a scanning probe microscope.

The viability of this proposal was proved in 1972 when the first NSOM was demonstrated using 3 cm microwave radiation [5]. An aperture of 1.5mm was used to detect the incident radiation, this was 1/20 of the illuminating wavelength. Aluminum grating samples of 1mm, 0.75mm and 0.5mm were prepared on glass slides to provide contrast for the microwave radiation and were all clearly resolved despite the diffraction limit of 3 cm; a resolution of $\lambda/60$.

The first scanning probe microscope was reported in 1981 when the scanning tunnelling microscope (STM) was demonstrated [6]. In 1986 Binnig and Rohrer were awarded the Nobel Prize in Physics *"for their design of the scanning tunnelling microscope"* [7]. This device combined the raster scanning principal demonstrated by the NSOM with the piezoelectric scanning device recommended by Synge in 1932. It coupled a sharp conducting tungsten tip to a piezoelectric scanning device used to manoeuvre the tip within several nanometres of a conducting surface. When a voltage is applied the electrons flow through the vacuum gap (potential barrier), separating the tip from the surface, most commonly termed quantum mechanical tunnelling. The tunnelling current J_T is exponentially dependent on the difference between the work function of the probe

and the sample, ψ, as well as the distance between the probe and sample, *s* [6],

$$J_T \propto e^{-A\psi^{1/2}s} \tag{1.1}$$

where A is a constant that is dependent on the appropriate quasi-free-electron mass. Assuming that the work function difference between the tip and surface remains constant then the tunnelling current *(1.1)* depends only on the tip-sample distance. This is the basis for topographical detection in STM. The tip is raster scanned across the surface and in every sample position the tunnelling current is kept constant by adjusting the height of the tip above the surface. The height of the tip above the surface is recorded by measuring the relative change in voltage applied to the z-axis piezoelectric positioning actuator from one location to another.

The high resolution of the STM is a consequence of the exponential dependence of the tunnelling current on the separation, *s*. For a typical work function difference, a change in topology of a few Ångstroms induces a change of up to three orders of magnitude in tunnelling current [6]. This, coupled with the ability of the piezoelectric positioning device to accurately place the tip within a fraction of a nanometre, allowed for atomic resolution imaging. Figure 1.1 shows an STM image of a chiral nanotube with atomic resolution; the positions of carbon atoms are clearly visible.

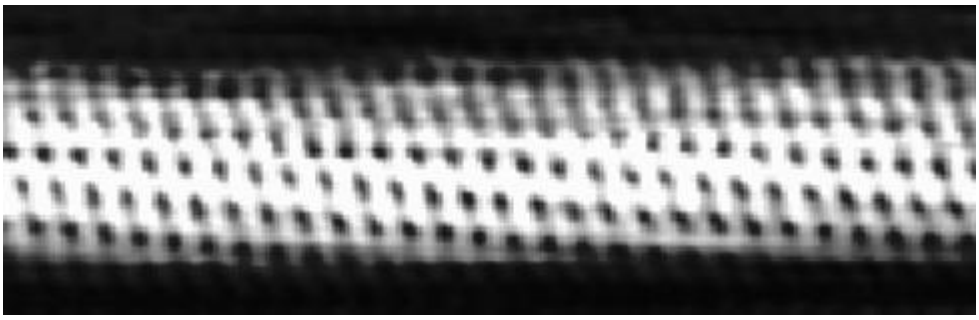


Figure 1.1: STM image of an atomically resolved chiral nanotube [8]

The invention of the STM dramatically improved the ability to inspect the surface of conducting and semiconducting materials, however insulating materials could not be imaged using this technique. In 1986 Binnig, Quate and Gerber published a paper describing an atomic force microscope (AFM) for imaging insulating surfaces [9]. This method was inspired by the stylus profilometer where a cantilever with a stylus is dragged across the sample surface. The AFM imaged the surface profile by detecting the force between the sample and a conductive cantilever with a sharp diamond tip. As the deflection of the cantilever is directly proportional to the force acting on it, the force can be measured indirectly by detecting the deflection. To detect the deflection an STM tip was placed above the cantilever and used as a feedback mechanism to keep the deflection on the cantilever constant, thus the topography of the sample could be determined by reading the height of the STM piezoelectric positioning device.

The deflection detection technique described by Binnig, Quate and Gerber was not ideal and others sought to improve the technique. In 1987 Martin, Williams and Wickramasinghe implemented an optical laser heterodyne interferometer to measure the deflection of the cantilever [10]. This device focused a laser on the top of the cantilever and measured the phase shift of the reflected optical radiation with respect to the

originating radiation to produce a measure of the cantilever deflection. A major improvement occurred in 1988 when Meyer and Amer published a method of detecting the deflection of a cantilever using a simple but effective beam bounce system [11]. This system used a tungsten wire electrochemically etched then bent to form a cantilever. A small mirror, 300 μm x 300 μm, was attached to the top of the cantilever to reflect the laser onto a split photodetector. The split photodetector detected the motion of the cantilever by sensing differences in optical illumination of both halves; a value that is modulated by the displacement of the cantilever (the split photodetector is discussed further in Section 2.3). This system has been widely adopted as a primary means of detecting the deflection of a cantilever. Modern Si cantilevers incorporate a reflective layer onto which a laser can be focused so the addition of a mirror is unnecessary.

The development of the AFM in 1986 spurred the development of many more scanning probe techniques. Of these, this thesis is most concerned with the electrostatic force microscope (EFM). In 1988 Martin, Abraham and Wickramasinghe modified an AFM to measure the electrostatic forces between a conducting AFM tip and an electrically charged sample [12]. This was accomplished by applying a DC voltage across the tip and sample and varying their separation. From this experiment the sensitivity to capacitance change was estimated to be approximately $4x10^{-20}$F [12]. Martin et al. found that an AC voltage was more convenient to measure the tip-sample capacitance. An AC voltage was applied between the tip and the sample and the induced oscillation on the cantilever was measured with an optical interferometer. The distance between the tip and sample was controlled using a feedback loop that attempted to maintain constant amplitude of

cantilever oscillation. It was estimated that the AC technique could achieve sensitivity to changes of capacitance on the order of $8x10^{-22}$ F [12]. These techniques provided a map of electrostatic force which could be mapped to localized voltage or changes of capacitance which offer a map of variation in dielectric constant.

In the same year that Martin et al. published their electrostatic imaging technique, Stern, Terris, Mamin and Rugar published a technique to deposit and image surface charge on insulating surfaces [13]. By adjusting the tip-sample distance, this technique used a feedback loop to maintain a constant force-gradient obtained from the vibration amplitude of the cantilever. To deposit a surface charge, a 100V, 25ms pulse was applied to the cantilever tip. The charge transfer mechanism was speculated to be corona discharge from the tip to the surface. With a charge deposited, the tip was then biased with respect to the sample and raster scanned across the surface. This technique detected three forces: the force due to the electrostatic interaction of the tip and the surface charge, the force due to the bias voltage between the tip and the sample and the van der Waals force acting between the tip and sample. The electrostatic force due to the surface charge was the desired signal; however the contrast of this signal could be enhanced by adjusting the bias of the tip to sample voltage. This technique illustrated that the local charge mobility of microscopic charges was much faster than the case of macroscopic charges by measuring the time required for the microscopic surface charge to dissipate and comparing it with the well known time of the macroscopic case.

The limiting factor of techniques that relied on the measurement of electrostatic forces

was the bandwidth imposed by the mechanical resonance of the cantilever. The maximum frequency that could be measured was limited by the cantilever frequency response [14]. A challenge is presented because most signals of interest change with much higher frequencies than that of the cantilever. As a solution to this problem, Bridges et al. developed a heterodyne EFM technique that allowed for measurement of high speed periodic signals [14,15]. This technique mixed a sinusoidal waveform at the resonant frequency of the cantilever with a periodic sampling waveform triggered at the same frequency as the signal to be detected; the resultant signal was then applied between the tip and sample. This gave several components that could be adjusted: the DC offset and frequency of the sinusoidal signal as well as the sampling waveform. An option suggested was to use a narrow pulse with an adjustable delay τ, as the sampling waveform, $V_S(t)$. In this case two terms are present in the equation of force at the cantilever resonant frequency; one known term containing a multiple of the DC offset of the applied sinusoidal waveform and the other a function of the voltage to be measured, $V_C(x,y,t)$. By nulling the total force at the cantilever resonant frequency reported by a lock-in amplifier (the amplitude of vibration at resonance is proportional to the force acting on the cantilever), the voltage to be measured $V_C(x,y,t=\tau)$, could be easily determined. This would provide the operator with a voltage measurement at the delay of the sampling waveform; to obtain a sample from the entire period of the voltage to be measured, the delay was swept from the beginning to the end of the periodic waveform being studied.

The heterodyne EFM technique provided a means to measure high speed changes in periodic signals applied to integrated circuits (IC). This was a very useful tool in

debugging problems with heavily integrated high speed ICs; it provided a means to measure the voltage present at any point on the surface of the IC with high spatial resolution. A problem with this technique would occur when a buried interconnect below the region of interest interfered with the measurement. This implies that the voltage being measured is not simply a surface phenomenon but the conducting tip on the cantilever is interacting with a *volume* of the sample. This volume is of interest when inspecting the dielectric properties of materials on and near the surface of a sample. The smaller the surface structures are, the more likely they will not be resolved from the substrate material. In this thesis this question will be addressed and an answer presented to the question of the volume of interaction.

1.2 Overview

In this thesis the size of the interaction volume in a sample subject to EFM probing is characterized. To this end, a simple dielectric grating sample was selected. The fields due to a tip in proximity to this sample were mathematically modelled and compared to the experimental results.

In chapter 2 the experimental theory and setup is presented. Background information regarding the electric force microscope and the heterodyne electrostatic imaging technique is presented along with the experimental setup. The equipment used in the experiments detailed in the document consists of a *Veeco Nanoscope IIIa* and *Enviroscope* controller connecting a workstation PC to the *Enviroscope* chamber. This chamber provided the piezoelectric scanning device and the cantilever deflection

detection system along with a sealed environmentally controlled chamber. This equipment also includes the frequency mixing devices and the lock-in amplifier used to detect the amplitude of vibration of the cantilever at resonance.

In chapter 3 the basis for the electrostatic model used in this thesis is presented. It starts by reviewing previous methods of estimating the field around a cantilever and selects the equivalent charge method. This method uses the fact that any charge distribution that results in the same field distributions are interchangeable. With this in mind the tip can be replaced by a series of point charges which is easier to model. The fields from these point charges are then calculated when in the presence of dielectric material as defined by the sample that is being modelled.

In chapter 4 the data that was captured to verify the model shown in chapter 3 is presented. It covers the calibration method used to convert from the cantilever deflection signal to the force acting on the cantilever, and general interpretation of the data as well as the data collection methods. The experimental data was then compared to the analytical model. The model was then used to estimate the lateral resolution of the technique as well as the dependence of the depth of the volume of interaction with the relative permittivity of the sample dielectric.

In chapter 5 the electrostatic modeling that was done to verify that the model is correctly implementing the electrostatic theory is discussed. This section discusses the use of *COMSOL*, a finite element analysis package that allows calculation of the various fields

of complex shapes that are not easily modeled. *COMSOL* was used to calculate the fields around a simulated tip and sample as well as determine the cause of discrepancies between the analytical model and experimental results.

2 Experimental Theory and Setup

2.1 EFM Background

The Electrostatic Force Microscope is a non-contact scanning probe technique developed from its predecessor, the Atomic Force Microscope, where a conducting tip is used to detect the electrical characteristics of a material. This technique uses the standard contact mode to determine the topography of the sample; the tip is brought in contact with the sample then scanned across the surface. The surface topology information is then used to scan the tip a set distance above the surface while a voltage is applied to probe the samples dielectric and conductive properties. When the charged tip approaches the surface of the test material a force is observed. This force is due to any surface charge that may exist as well as the polarization of the dielectric material.

The motion of the cantilever when the probe is not in contact with the surface obeys the second order differential equation for forced harmonic oscillation, (2.1) [16],

$$m\frac{\partial^2 z}{\partial t^2} + \frac{\omega_0 m}{Q}\frac{\partial z}{\partial t} + kz = F + F_1\zeta \tag{2.1}$$

where m is the mass of the cantilever, $z = z_0+\varsigma_\Omega$ is the position of the tip above the surface, ς_Ω is the oscillatory component of the cantilevers position described at resonance by $A_v sin(\Omega t+\varphi_1)$, ω_0 is the resonant frequency of the cantilever, Q is the quality factor of the system and k is the spring constant. At resonance ($\Omega=\omega_0$) this equation simplifies to (2.2) where k' is the effective spring constant which accounts for the force derivatives [16].

$$\left[k' - \omega^2 m + i\frac{m\omega_0\omega}{Q}\right]\zeta_\Omega = F_\Omega \tag{2.2}$$

Equation (2.2) can be solved for ζ_Ω, which is a function of the amplitude of vibration at resonance, A_v. At resonance the amplitude of vibration can be approximated by [16]:

$$A_v \approx \frac{Q}{k}\left|F_\Omega\right| \tag{2.3}$$

This shows a linear relationship between the amplitude of vibration at resonance of the cantilever and the force acting on the cantilever, which is stable, provided that the quality factor and spring constant do not change during operation. The quality factor is defined by the damping effects of the environment such as vacuum quality or air density. In the experiments described in this thesis, the vacuum quality does slowly drift over time but this variation was not sufficiently large to cause a noticeable effect. The spring constant is based on physical properties of the cantilever and varies only when in close proximity to the surface. Relation (2.3) is useful as a way of calculating the force acting on the tip by measuring the amplitude of vibration of the cantilever at its resonant frequency.

2.2 Heterodyne Electrostatic Imaging

The experimental work performed utilized an imaging technique developed to perform measurements of high speed changes of the polarization of dielectric material. The change in polarization is typically limited by the mechanical bandwidth of the cantilever. This technique allows changes in charge to be measured at much higher frequencies when compared with the mechanical resonant frequency of the cantilever. To achieve this, a high frequency signal is amplitude modulated at half of the resonant frequency (see the

discussion around (2.4)) of the cantilever and then applied to the tip [17]. Depending on the application the RF signal may be applied directly to the sample to induce, for example, a surface acoustic wave [18].

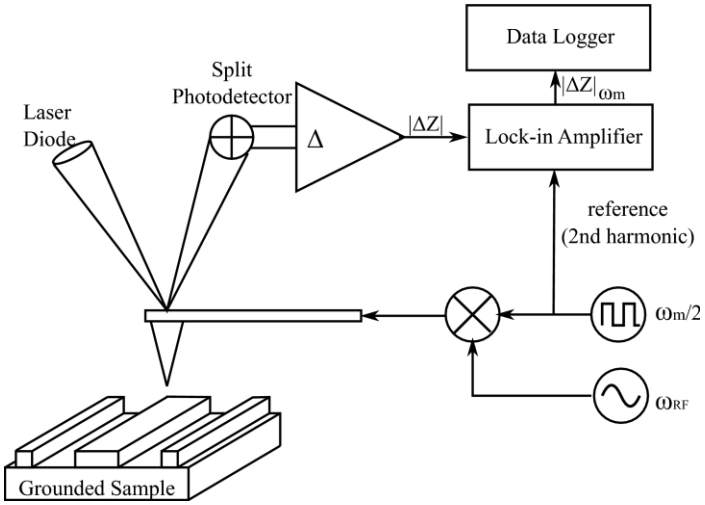


Figure 2.1: Experimental setup. The cantilever voltage is driven by an applied amplitude modulated signal. The change in position of the cantilever is detected using a beam bounce system and sent to a lock-in amplifier to be analyzed and recorded by a computer.

The cantilever is driven by applying an amplitude modulated signal shown schematically in Figure 2.1. This signal is designed to drive the cantilever at its resonant frequency as well as stimulate the sample at frequencies of interest. The high frequency component is chosen arbitrarily and depends on the sample that is to be probed. The low frequency component is chosen based on the cantilever being used and is equal to half of its resonant frequency. The relation of one half is due to the equation of the force on the tip (2.4) [16,17].

$$F_z = \frac{1}{2}\left(\frac{\partial C}{\partial z}\right)V^2 \tag{2.4}$$

This equation shows the force acting on the cantilever in the vertical direction is related to the derivative of the capacitance between the tip and sample as well as the square of

the voltage signal applied to the tip. As a result, the force acting on the tip that will drive the cantilever, is dependent on the square of the applied voltage. The applied voltage can be represented as the product of two sinusoidal signals at frequency $\omega_m/2$ and ω_{RF}. The square of the applied voltage is calculated as shown in (2.5).

$$V = \cos\left(\frac{\omega_m}{2}t\right)\cos\left(\omega_{RF}t\right) \tag{2.5}$$

$$V^2 = \cos\left(\frac{\omega_m}{2}t\right)^2\cos\left(\omega_{RF}t\right)^2 = \left(\frac{1+\cos\left(\omega_m t\right)}{2}\right)\left(\frac{1+\cos\left(2\omega_{RF}t\right)}{2}\right)$$

$$V^2 = \frac{1}{4}\left[1+\cos\left(\omega_m t\right)+\cos\left(2\omega_{RF}t\right)+\frac{1}{2}\left(\cos\left(2\omega_{RF}t+\omega_m t\right)+\cos\left(2\omega_{RF}t-\omega_m t\right)\right)\right]$$

$$V^2 = \frac{1}{4}\left[1+\cos\left(\omega_m t\right)+ high\ \ frequency\ \ components\right]$$

The first term of V^2 is purely ω_m, while the remaining terms are all near the high frequency component, ω_{RF}. Note that the low frequency component, ω_m, is double the applied frequency. This term is directly responsible for stimulating the cantilever at resonance and is chosen to match the resonant frequency of the cantilever.

The deflection signal generated by the split photodetector was used as an input to a lock-in amplifier. The lock-in amplifier provided an output signal that was proportional to the amplitude of the deflection signal at the resonant frequency of the cantilever. The second harmonic of the modulation frequency (i.e. ω_m) was passed to the lock-in amplifier as the reference frequency. The output of the lock-in amplifier was then fed into the computer to be recorded by the software.

The mixer depicted in Figure 2.1 was a Mini-Circuits ZASWA 2-50 high speed switch driven at a frequency of $\omega_m/2$. This setup essentially amplitude modulates a square wave with a sinusoidal signal. The effect of this was the addition of higher order harmonics of the low frequency signal and has no effect on the operation of the imaging technique.

2.3 Experimental Setup

The experimental apparatus used to conduct these experiments was a *Vecco di EnvroScope* connected to a computer with a *NanoScope IIIa* controller. The *EnviroScope* provides a small chamber in which the sample and tip can be placed under vacuum. This chamber houses the deflection sensor and optics and provides a means of changing the sample and making electrical connections.

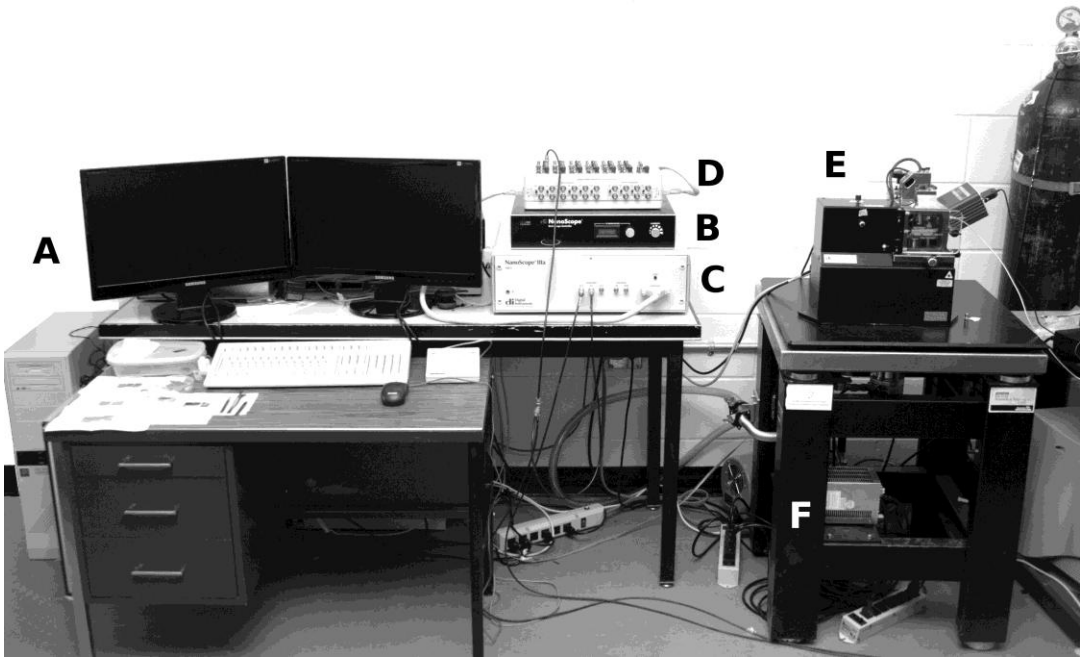


Figure 2.2: Experimental Apparatus consists of a personal computer (A) connected to a Veeco EnviroScope controller (B) and a NanoScope IIIa AFM controller (C) connected to a breakout box (D). The controllers operate the EnviroScope (E) which is isolated on an air table (F).

The cantilever used for these experiments required a conductive coating on the contacting

side to which the voltage signal can be applied. The tips chosen were the NSC18/Ti-Pt. These silicon cantilevers were coated by the manufacturer with 20 nm of titanium followed by 10 nm of platinum. The voltage signal was routed though an SMA connector on the sidewall of the vacuum chamber then to a cantilever clamp with a conductive path to the tip. Once the tip was installed in the *EnviroScope* the sample was mounted directly below the tip.

The TGZ series sample grating, the sample that was selected for this work, was grounded with respect to the voltage signal that was applied to the tip. To ensure proper grounding, conductive silver epoxy was used to attach the sample grating to a sample stage. This stage was then mounted on a conductive magnetic puck that was used to mechanically support the sample on the *EnviroScope's* stage as well as provide a conductive path to ground (the housing of the vacuum chamber).

To detect the force acting on the tip, the amplitude of vibration was measured using a beam bounce system where a laser is focused on the back of the cantilever and reflected back to a split photodetector, represented graphically in Figure 2.3. The photodetector measures the optical power incident on its four quadrants, producing signals proportional the sum of all quadrants (A+B+C+D), the difference between the top and bottom halves (A+B-C-D), and the difference between the left and right halves (A+C-B-D). This allows the microscope to measure the vertical and horizontal deflection signals as well as the total sum signal which is an indication of how well the laser is aligned with the cantilever tip. When the beam is centred on the detector the optical power is equal on all quadrants.

When the tip is deflected away from the surface, the beam shifts from the centre position toward the top half of the detector. In this case the signal from the activated quadrants will become stronger and the signal from the opposing quadrants will weaken, thus indicating the beam has shifted and the tip has moved. The output of the photodetector system provides the controller with a measure of the deflection of the cantilever in both the vertical and horizontal direction and will correspond to the movement of the tip from its neutral position. The vertical deflection signal is utilized when the tip is engaged to the sample surface. The tip starts above the surface and is moved toward it, before the tip makes contact, the vertical deflection signal will remain constant. Once the tip makes contact with the surface, the deflection signal will increase due to the bending of the cantilever until the desired deflection is reached. At this point the microscope will raster the tip across the surface using a control system to maintain the desired deflection by adjusting the height of the piezoelectric positioning tube; the surface topology is determined by recording the height of the piezo.

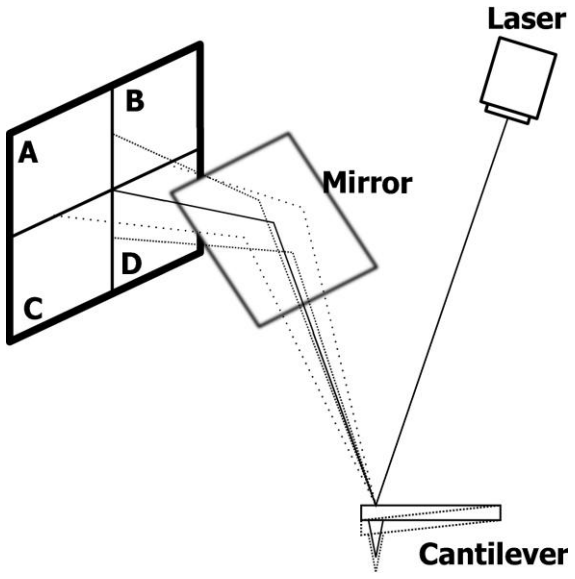


Figure 2.3: Beam bounce system used to detect horizontal and vertical deflection using a four quadrant split photodetector.

The amplitude of oscillation is important in this method because it can be related to the force by (2.3). This force reflects the electrostatic attraction between the tip and sample; the calculation of which is dependent on the quality factor. Air causes a significant damping effect on the cantilever which is mathematically observed in the quality factor, *Q*. In air, the cantilevers used had quality factors on the order of 10^2. This left a resonant peak with a very low signal to noise ratio. To increase the sensitivity of this system it was desirable to operate in a vacuum which, as a consequence of removing the damping due to air, results in a sharper (narrower) resonant peak. This is typically characterized as an increase in the quality factor of the system.. The width of this peak is important as the cantilever approaches the sample surface, the resonant frequency will shift with the loading of the cantilever due to the van der Waals attractive forces (this issue is the basis for *tapping mode* operation). If the cantilever is not being driven at its resonance frequency the lock-in amplifier will not report the correct amplitude of vibration because its reference signal is generated from the driving frequency applied to the cantilever. To prevent the need for external correction it is desirable to operate with a sufficiently narrow resonant peak to provide enough sensitivity, while maintaining a sufficiently wide resonant peak that a slight shift in resonant frequency will have a minor effect on the output. This is effectively a trade-off between sensitivity and stability.

Figure 2.4 shows a plot of the quality factor versus pressure. This plot was created by allowing the pump to reach steady state pressure, around 10^{-5} Torr, closing the vacuum valve and allowing the chamber to gradually drift back to atmospheric pressure. At each

pressure in Figure 2.4, spectra representing an average of 50 samples were downloaded from the spectrum analyzer. The precision of these measurements, 2 Hz, represented the frequency resolution (bin size) setting of the spectrum analyzer. It was found experimentally that a quality factor on the order of a few thousand was a desirable operating point; a fair trade off between sensitivity and stability. This operating point was achieved by using the priming pump and not engaging the turbo pump, after approximately 15 minutes the pressure stabilized at approximately 10^{-1} Torr.

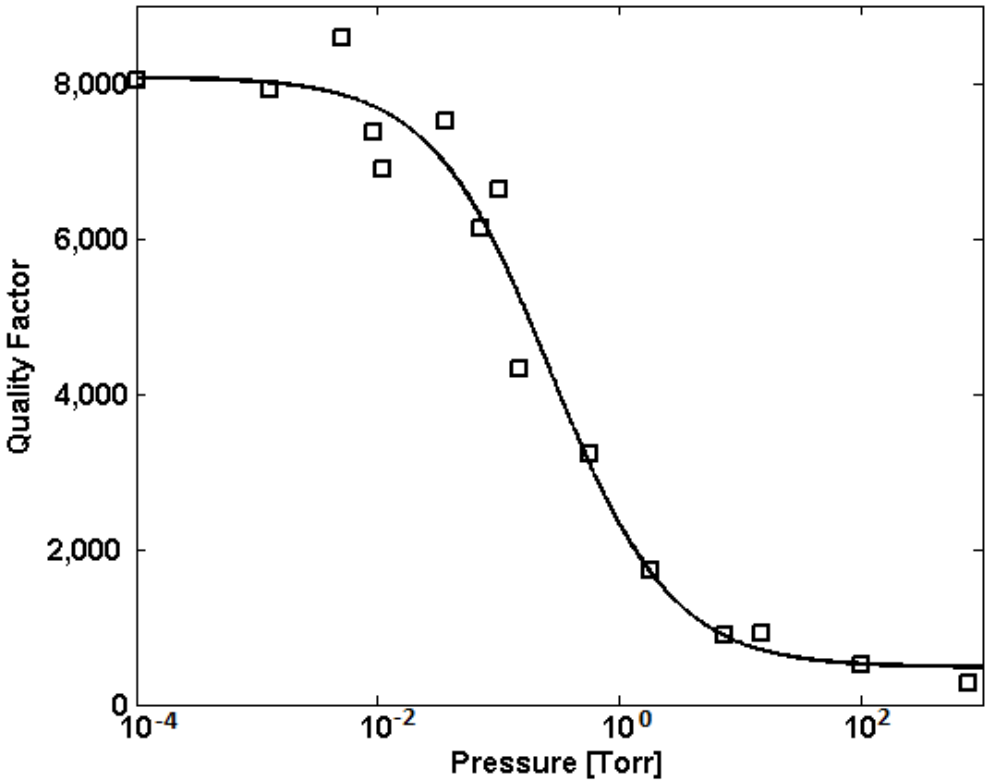


Figure 2.4: Quality factor of the cantilever versus the air pressure in the vacuum chamber. The major source of error is due to the finite width of frequency bins of the spectrum analyzer.

To begin a series of sample collections, the sample was arranged such that the troughs of the TGZ series grating were parallel to the slow scan axis. This is done to prevent discontinuities in the electrostatic scan when the tip crossed the boundary between the

sample step and the substrate. These discontinuities can be quite large in comparison to the meaningful data and so must be prevented. The tip was then randomly placed above a section of the sample that optically appeared to be free of debris. The priming vacuum pump was engaged and the chamber pressure stabilized over a period of several minutes. Once the vacuum level was near the desired operating point, the tip was engaged as described previously.

The TGZ sample gratings have a 3μm period so a contact mode scan was initially performed covering a 10 μm square. This was done at a relatively high scan rate of 1-2Hz. The image created by this initial scan was used to level the sample and obtain a perspective on what was in the neighbourhood of the tip when the scan was being completed. Once a suitable step was located the scan size was decreased to image only the edge of a single step, the slow scan axis was disabled and lift mode was enabled. By disabling the slow scan axis, the image created was representative of the average value of a single line on the surface of the sample rather than a two dimensional area. This provided statistical relevance to each sample point on the scan line by calculating the mean value of the response above the surface.

The decision to image only the edge of a step was made to increase the time spent above any data point while in lift mode. The relatively large quality factor required to operate provides a compromise; a large quality factor is required to pick the resonant peak out of the background noise, however, it causes the cantilever to oscillate with little damping so a longer period of time is required to allow the cantilever to settle over every data point

captured.

Once the scan process was started, the cantilever's resonant peak from the deflection signal was observed using a SR760 FFT spectrum analyzer, sampling the signal at 100 kHz. If a shift in resonant behaviour of the cantilever was observed then a manual adjustment of the driving frequency would be made. This adjustment would ensure that the driving frequency always corresponded to one half of the resonant frequency of the cantilever, thus providing the lock-in amplifier with an accurate reference.

3 Electrostatic Modelling of EFM Setup

3.1 Introduction

The purpose of the model introduced in this chapter is to simulate the experimental setup and to provide insight into the fields that surround the tip and sample. Specifically, an estimate of the volume of test material interacting with the tip is desired. To accomplish this, a model is outlined that estimates the total force acting on the cantilever when the tip is centred directly above a peak (Figure 3.1 A) and a valley (Figure 3.1 B) on the sample grating, TGZ-01, 02 & 03 manufactured by MikroMasch [19]. The comparison between experimental data and the model enables estimation of the volume of interaction.

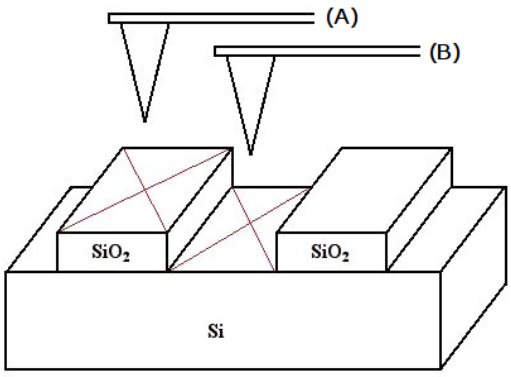


Figure 3.1: TGZ series sample grating used to validate the model. A) Tip centred above SiO2 grating. B) Tip centred above Si substrate

The voltage entirely characterizes a given electrical and geometrical setup and is normally found by solving Laplace's Equation. The solution to LaPlace's Equation will yield the voltage at every location in the space surrounding the tip. In order to find the forces associated with a given electrical and geometrical setup the voltage arising from the tip must be known. The total force can be derived from the electric field, displacement field and the polarization density which can all be derived from this

voltage.

The most basic case would be to solve Laplace's Equation with a conducting AFM tip in proximity to a grounded planar electrode. At first glance this problem appears straight forward but to date there is no general analytic solution despite attempts to estimate it [20]. Chung et al. use Legendre Functions of non-integral order to find an exact solution of the near field and estimates the far field with that of a tip in contact with the ground plane [20]. Patil et al. used the prolate spheroidal coordinate system to approximate the tip as a hyperbola, although this technique is only valid when the tip-sample distance is on the order of the tip radius [21].

When the tip is within a few tip radii of the conducting surface, the effects of the cone can be ignored. In this case, a common practice is to model the tip as a sphere placed above the ground plane as is done by Terris et al. [22]. Jeffery used the bispherical coordinate system to find an exact solution to the Laplace equation under these conditions [23]. An extension of this idea is to use a point charge located above the surface to model the sphere [24]. When the point charge is sufficiently far from the ground plane, an equipotential surface can be considered roughly spherical. The problem with the sphere model is that it only represents a part of the tip and the entire cone should be considered for a good estimation of the total force seen by the cantilever.

Hudlet [25] modeled the tip as a cone with a spherical tip then broke down the surface into infinitesimal facets. The field due to each facet was assumed to be the same as the

field due to two infinite planes with the same orientation as the facets. The total field was then found by the superposition of the fields due to each facet. Belaidi et al. reviewed and compared a series of analytical models to the equivalent charge model (ECM) [24].

The ECM replaces the tip with a series of point charges on the vertical axis with magnitudes such that the surface of the tip is at a constant voltage [24,26,27]. When a conducting tip is placed above a ground plane, the method of images enables replacement of the ground plane by a series of equal but opposite charges. In this case the voltage at any point can be found using [24]:

$$V(r_m) = \frac{1}{4\pi\varepsilon_0}\sum_{i=1}^{N}\left(\frac{Q_i}{|r_m - r_i|} - \frac{Q_i}{|r_m + r_i|}\right) \tag{3.1}$$

where Q_i is the i^{th} point charge, $\boldsymbol{r_m}$ is the point at which the voltage is to be calculated, and $\boldsymbol{r_i}$ is the location of the i^{th} point charge. Equation (3.1) is used to solve for Q_i by creating a series of M equations with N unknowns. By selecting M test points on the surface of the tip, N charge positions at $\boldsymbol{r}_i$ along the z-axis, and $V(\boldsymbol{r}_m)=V_0$ for the tip voltage, an overdetermined system (M>N) can be created that can be solved using the least mean square method of error minimization. With all Q_i and $\boldsymbol{r}_i$ known, the voltage at any point can be found and plotted as shown in Figure 3.2.

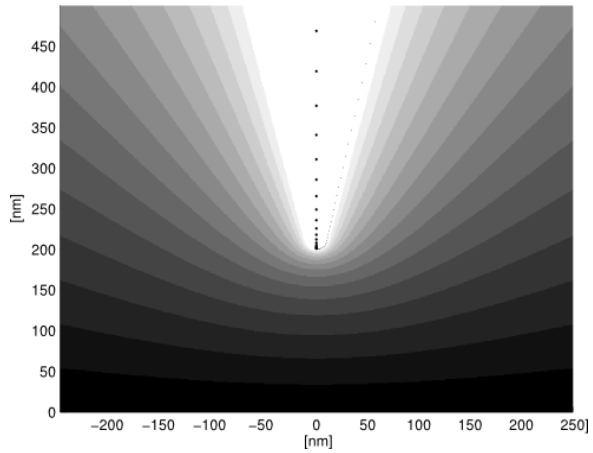


Figure 3.2: Equipotentials (voltage) found using the ECM. Point charges and test points are marked.

This method works well but cannot be used without modification to predict the fields found in the present study. The TGZ sample grating will cause the fields to deform at the interfaces between the two different dielectric materials. Despite this, the ECM was used as a basis for the model described in the following sections.

3.2 Field due to a Single Point Charge

The ECM presented in [24] consisted of an infinite grounded plane with the tip located above it and no ability to account for dielectric material. The ECM in [26,27] allowed for limited insertion of dielectric material; the tip charges are placed above an infinite dielectric sheet that rests on a ground plane. To model the TGZ series sample gratings the silicon substrate, as well as a layer of silicon dioxide, the tip and the ground plane must all be considered. The ECM presented in [27] suggests the use of Green's functions to model multiple layers of dielectric material and this method was chosen.

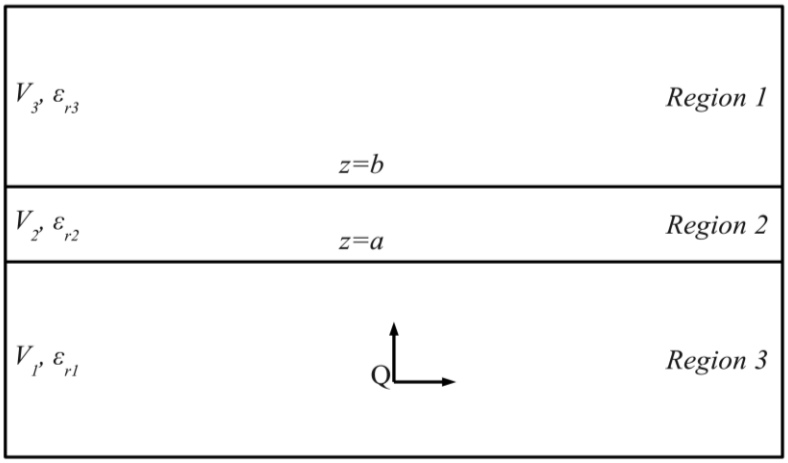


Figure 3.3: A point charge Q is located at the origin with two dielectric boundaries at z=a and z=b. This forms three distinct regions, region 1, 2 & 3.

Smythe outlined the following procedure in [28]; a point charge of Q is located at the origin in proximity to two dielectric boundaries forming three regions with boundaries located at $z=a$ and $z=b$. The geometry is presented graphically in Figure 3.3. To develop a solution for the Laplace equation in all three regions, the first case considered was that without any dielectric material present. The solution to this case yielded [28]:

$$V\left(r\left(\rho,z\right)\right)=\frac{Q}{4\pi\varepsilon_0}\int J_0\left(k\rho\right)e^{\left(-k|z|\right)}\mathrm{d}k=\frac{Q}{4\pi\varepsilon_0}\frac{1}{\sqrt{\rho^2+z^2}}=\frac{Q}{4\pi\varepsilon_0|r|} \tag{3.2}$$

With the dielectric configuration used, the electric field from a point charge placed at the origin in region three caused the molecules of the dielectric material to polarize, which in turn created a secondary electric field that summed with the primary electric field in the region. This secondary electric field can be modelled by adding a second term to (3.2). It should be noted that any function of k can be inserted inside the integral and the result will always be a solution to Laplace's Equation because the integral only involves ρ and z [28]. This property was used to determine the prototype voltage found in (3.3).

$$V_1(\rho,z)=\frac{Q}{4\pi\varepsilon_0}\left(\int J_0(k\rho)e^{(-k|z|)}\mathrm{d}k+\int A(k)J_0(k\rho)e^{(kz)}\mathrm{d}k\right) \tag{3.3}$$

Similarly, V_2 and V_3 can be written [28]:

$$V_2(\rho,z)=\frac{Q}{4\pi\varepsilon_0}\left(\int B(k)J_0(k\rho)e^{(-kz)}\mathrm{d}k+\int C(k)J_0(k\rho)e^{(kz)}\mathrm{d}k\right) \tag{3.4}$$

$$V_3(\rho,z)=\frac{Q}{4\pi\varepsilon_0}\int D(k)J_0(k\rho)e^{(-kz)}\mathrm{d}k \tag{3.5}$$

These equations contain four unknown functions of *k*. To determine the unknowns the dielectric boundary conditions were considered. At a dielectric boundary both the voltage and the normal components of the electric displacement must be piecewise continuous, this is a direct result of Gauss's Law [26,28,29]. Assuming the absence of bound charge at the dielectric boundaries, the four boundary conditions for the present case are:

$$V_1(\rho,a)=V_2(\rho,a) \tag{3.6a}$$

$$\varepsilon_{r1}\frac{dV_1}{dz}\Big|_{z=a}=\varepsilon_{r2}\frac{dV_2}{dz}\Big|_{z=a} \tag{3.6b}$$

$$V_2(\rho,b)=V_3(\rho,b) \tag{3.6c}$$

$$\varepsilon_{r2}\frac{dV_2}{dz}\Big|_{z=b}=\varepsilon_{r3}\frac{dV_3}{dz}\Big|_{z=b} \tag{3.6d}$$

Using these boundary conditions, a series of four equations and four unknowns may be assembled that will allow *A*, *B*, *C* & *D* to be determined. Using these results and (3.7) & (3.8), V_1, V_2 and V_3 can be solved as a function of the geometrical and electrical parameters. With this knowledge of the voltage, the method of images as well as a shift of the coordinate system was used to mirror the model about the *z=0* plane as illustrated in

Figure 3.4. This caused the *z=0,* plane to be a contour of zero voltage and model the ground plane. The total voltage in Regions 1, 2 & 3 was, therefore, the superposition of the voltage due to the charge *Q* and the image charge -*Q*. The results of these calculations are found in (3.9); a sample calculation of these voltages is shown in Figure 3.5.

$$\int J_0(k\rho)e^{(-kz)}\mathrm{d}k = \frac{1}{\sqrt{\rho^2 + z^2}}, z > 0 \tag{3.7}$$

$$\frac{1}{1+x} = \sum_{i=0}^{\infty}(-1)^i x^i \tag{3.8}$$

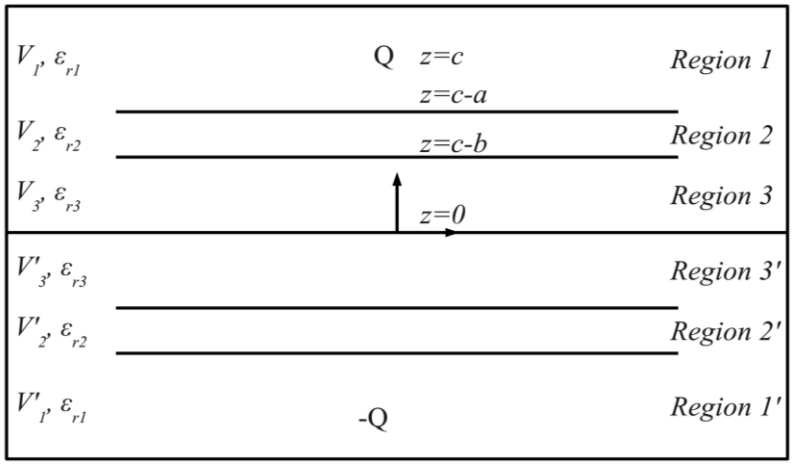


Figure 3.4: Two equal but opposite point charges are mirrored about the plane z=0. The dielectric configuration is also mirrored about this plane.

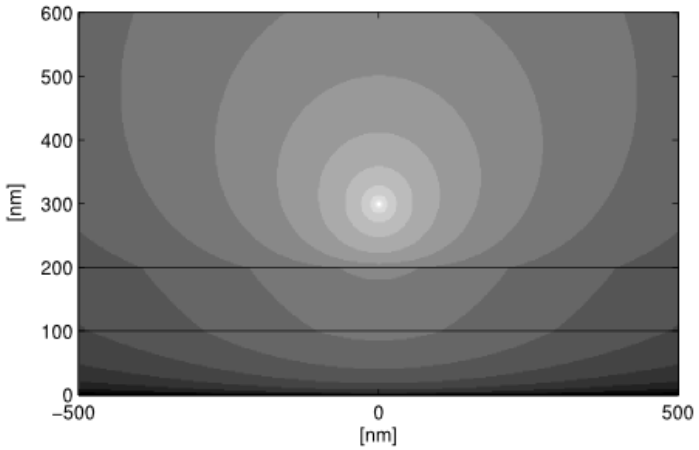


Figure 3.5: Equipotentials (voltages) due to a single point charge about three dielectric regions above a ground plane. From top to bottom, $\varepsilon_{r1}=1$, $\varepsilon_{r2}=12$ & $\varepsilon_{r3}=4$.

$$\frac{4\pi\varepsilon_0}{Q}V_1 = \frac{1}{\sqrt{\rho^2+(z+c)^2}} + \sum_{i=0}^{\infty} A^i \left[\frac{R}{\sqrt{\rho^2+r^2}} + \frac{D}{\sqrt{\rho^2+d^2}} - \frac{E}{\sqrt{\rho^2+e^2}} \right] \tag{3.9a}$$

$$\frac{4\pi\varepsilon_0}{Q}V_2 = \sum_{i=0}^{\infty} A^i \left[\frac{F}{\sqrt{\rho^2+f^2}} + \frac{G}{\sqrt{\rho^2+g^2}} - \frac{E}{\sqrt{\rho^2+e^2}} \right] \tag{3.9b}$$

$$\frac{4\pi\varepsilon_0}{Q}V_3 = \sum_{i=0}^{\infty} A^i \left[\frac{H}{\sqrt{\rho^2+h^2}} - \frac{E}{\sqrt{\rho^2+e^2}} \right] \tag{3.9c}$$

Where the constants in (3.9) are defined by:

$$A = (-1)\left(\frac{\varepsilon_{r1}-\varepsilon_{r2}}{\varepsilon_{r1}+\varepsilon_{r2}}\right)\left(\frac{\varepsilon_{r2}-\varepsilon_{r3}}{\varepsilon_{r2}+\varepsilon_{r3}}\right)$$

$$R = \left(\frac{\varepsilon_{r2}-\varepsilon_{r3}}{\varepsilon_{r2}+\varepsilon_{r3}}\right) \qquad r = (z-c)+2\mathrm{b}+2(b-a)i$$

$$D = \left(\frac{\varepsilon_{r1}-\varepsilon_{r2}}{\varepsilon_{r1}+\varepsilon_{r2}}\right) \qquad d = (z-c)+2\mathrm{a}+2(b-a)i$$

$$E = \frac{4\varepsilon_{r1}\varepsilon_{r2}}{(\varepsilon_{r1}+\varepsilon_{r2})(\varepsilon_{r2}+\varepsilon_{r3})} \qquad e = (z+c)+2(b-a)i$$

$$F = \frac{2\varepsilon_{r1}}{(\varepsilon_{r1}+\varepsilon_{r2})} \qquad f = -(z-c)+2(b-a)i$$

$$G = \frac{2\varepsilon_{r1}(\varepsilon_{r2}-\varepsilon_{r3})}{(\varepsilon_{r1}+\varepsilon_{r2})(\varepsilon_{r2}+\varepsilon_{r3})} \qquad g = (z-c)+2\mathrm{b}+2(b-a)i = r$$

$$H = \frac{4\varepsilon_{r1}\varepsilon_{r2}}{(\varepsilon_{r1}+\varepsilon_{r2})(\varepsilon_{r2}+\varepsilon_{r3})} = E \qquad h = -(z-c)+2(b-a)i = f$$

*a, b & c and ε_{r1}, ε_{r2} & ε_{r3} are defined in Figure 3.4.

3.3 Equivalent Charge Model

With the knowledge of the field due to a single point charge in the presence of dielectric sheets, the field of a conical AFM tip may be developed in the presence of these same dielectric sheets. To do this, the tip was modelled as a series of point charges distributed along the z-axis. To create the equipotential surface, a series of test points located on the tip surface and point charges were chosen such that the equipotential surface was maintained at V_0.

The charge positions had to be chosen arbitrarily but the point of the AFM tip is orders of magnitude smaller than the base, so charges were preferentially assigned nearer to the tip using the quartic relation of (3.10).

$$t = \left(\frac{n-1}{N_c-1}\right)^4 \tag{3.10}$$

In this relation, n is the n^{th} point charge of a total of N_c point charges and t will lie between zero and one. The exponent of 4 was chosen arbitrarily to ensure that there were many more point charges near the tip than the base. Using this relationship, the N_c points along the line defined by (3.11) were found.

$$z = \left(h - \frac{r_0}{10} \right) t + z_o + \frac{r_0}{10} \tag{3.11}$$

This line is defined from $0<t<1$, where h is the tip height (20.25μm), r_0 is the tip radius (10 nm) and z_0 is the absolute position of the tip above the ground plane. The $r_0/10$ term prevents the point charges from being placed on the surface of the probe, which would cause a singularity at that point.

The test positions were calculated using a similar method. Again the quartic relation of (3.10) is used to find t (although N_t, the number of test charges, is substituted for N_c). To determine the boundary between the spherical and the conical tip surfaces the portion of the total length that corresponds to the the length of the spherical surface needs to be defined. This point, *sw*, is where the switch from the spherical distribution formula to the conical distribution formula occurs and is defined as (see Figure 3.6):

$$sw = \frac{length\ of\ arc}{length\ of\ arc + length\ of\ cone} = \frac{(\pi/2 - \theta_0) r_0}{(\pi/2 - \theta_0) r_0 + \left(\frac{h}{\cos(\theta_0)} - \frac{r_0}{\tan(\theta_0)} \right)} \tag{3.12}$$

For the points that lie on the spherical part of the tip model, the coordinates were calculated using:

$$r_t = \begin{bmatrix} r_0\cos(\theta') \\ r_0\sin(\theta') + z_0 + r_0 \end{bmatrix} \tag{3.13}$$

$$\theta' = \left(\frac{\pi}{2} - \theta_0\right)\frac{t}{sw} + \frac{3\pi}{2} \quad 0 < t < sw$$

For the points that lie on the conical part of the tip model, the coordinates were calculated using:

$$r_t = \begin{bmatrix} r_{tp} \\ r_{tz} \end{bmatrix} = \begin{bmatrix} \frac{(h\tan(\theta_0) - r_0\cos(\theta_0))}{1 - sw}(t-1) + h\tan(\theta_0) \\ \left(\frac{h - r_0(1-\sin(\theta_0))}{h\tan(\theta_0) - r_0\cos(\theta_0)}\right)(r_{tp} - h\tan(\theta_0)) + h + z_0 \end{bmatrix} \quad sw < t < 1 \tag{3.14}$$

Using these calculations, the charge positions and the test positions can be found for any given set of geometrical parameters. Figure 3.2 shows an example plot with the test points and point charge positions marked.

With the charge locations and test points clearly defined, the magnitude of the charges was revealed using (3.9a). This equation was solved for V_1; since the relation between V_1 and Q is linear, Q is factored out. (3.15) shows this result summed for all point charges.

$$V(r_i) = \sum_{j=1}^{Nc} V_1(Q_j, a_i, b_i, c_i) = \sum_{j=1}^{Nc} Q_j V_1(1, a_i, b_i, c_i) = V_0 \quad 1 < i < N_t \tag{3.15}$$

This equation can be written for every i^{th} test point to obtain N_t equation with N_c unknowns. Provided that $N_t > N_c$, this system can be solved for all Q using the least mean squares method of error minimization.

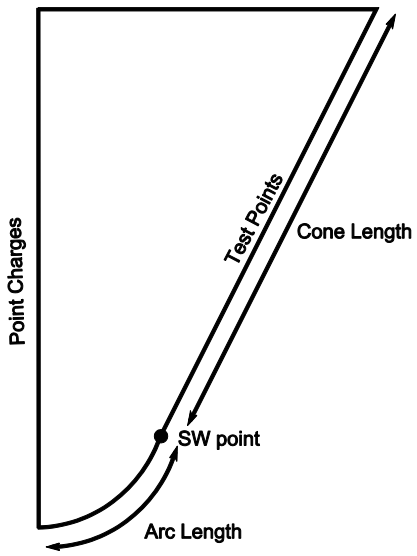


Figure 3.6: Tip geometry illustrating the switch over point between the conical and spherical distributions

Although the distribution of the point charges and the test points have been determined, and from this the value of the point charges as a function of the tip voltage, V_0, have been calculated there has been no discussion of how to choose N_c and N_t. These values are arbitrary but may be chosen based on different reasoning. The number of point charges will affect the overall processing time required to find the fields at any given point, a process that is required to be repeated several millions of times to obtain any useful data. An Intel Core 2 Duo running at 1.8 GHz took approximately 210 μs per point charge to calculate the fields at a point. This relation scaled linearly, if the number of point charges doubled, the calculation time would double. The number of point charges also affected the error. The assumption that the fields due to the tip are equivalent to the fields due to the point charges enabled the estimation of the root mean square (RMS) error from the voltage difference between the tip voltage at the test points, and was calculated using (3.16).

$$E_{RMS} = \sqrt{\frac{1}{N_t}\sum_{i=1}^{N_t}\left(V_1(r_i) - V_0\right)^2} \tag{3.16}$$

In Figure 3.7, this error has been plotted in the range of 2 to 400 point charges, showing that an increased number of point charges asymptotically decreases the RMS error, neglecting the available processing power. For the simulations run N_c=40 was chosen to balance processing time and RMS error.

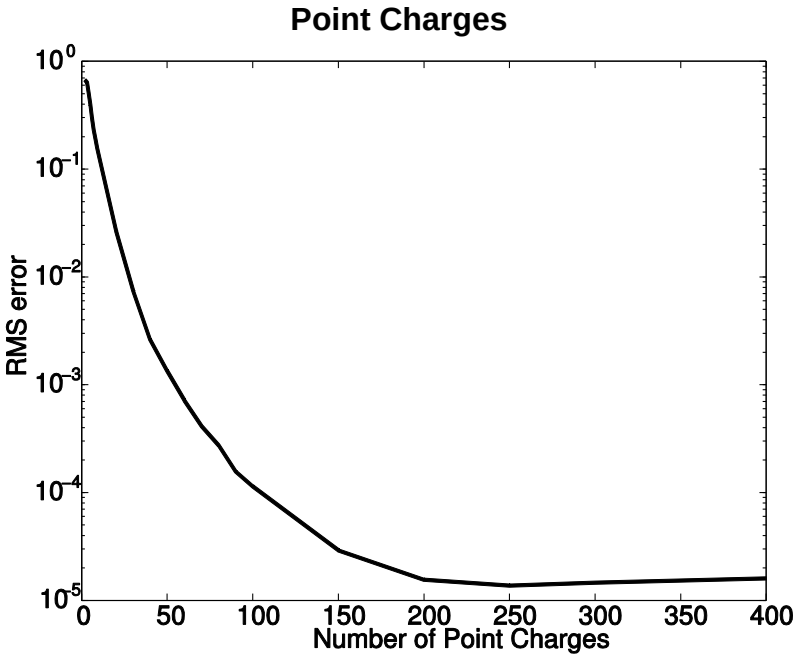


Figure 3.7: RMS error of the equivalent charge model varies with the number of point charges used to model the tip.

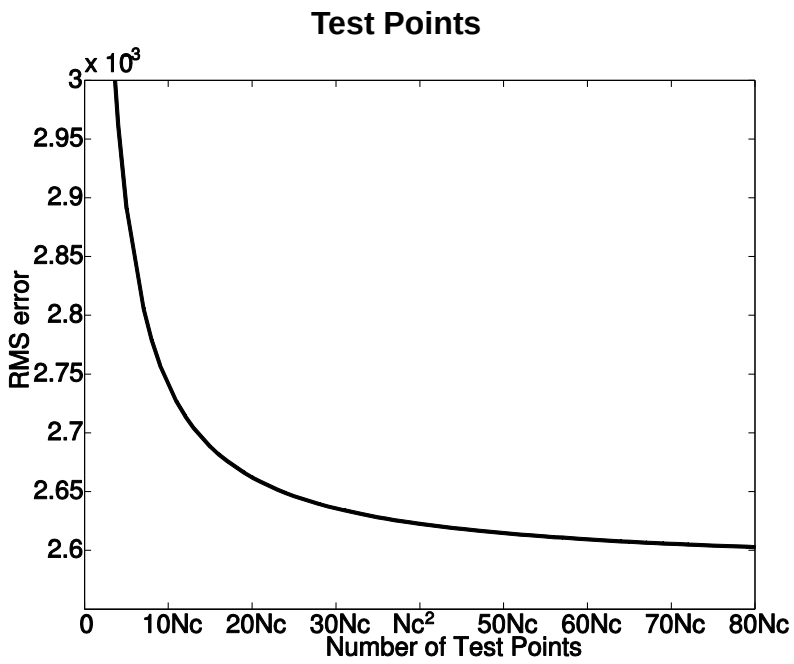


Figure 3.8: RMS error of the equivalent charge model varies with the number of test points used. This plot was generated with N_c=40.

When choosing the number of test points distributed on the tip surface, N_t, it was found that many more test points than point charges were desirable as it significantly reduced the RMS error. Figure 3.8 shows a plot of the RMS error for 40 point charges as a function of increasing test points. It was clear that the number of test points should be greater than the number of point charges however, the error approaches its asymptote well before $N_t=N_c^2$. This may be an excessive number of test points, however this process required only a short time compared to the time required to perform post processing calculations using the model. For example, on the same computer mentioned above, it took approximately 26 seconds to compute the point charges compared with almost 10 minutes to perform post processing tasks.

3.4 Post Processing

To validate the model its output was generated and compared to the experimental results.

To verify the model, it was decided to use the total force seen by the tip over the silicon substrate and the silicon dioxide grating. In order to calculate the total force acting on the tip in any given geometry the electrostatic Maxwell stress tensor was used. In the two dimensional case, this is defined by [30]:

$$T_{ij} = D_i E_j - \frac{1}{2} D \cdot E \delta_{ij} \quad \text{or} \quad T = \begin{bmatrix} D_\rho E_\rho - \frac{1}{2} D \cdot E & D_\rho E_z \\ D_z E_\rho & D_z E_z - \frac{1}{2} D \cdot E \end{bmatrix} \tag{3.17}$$

The Maxwell stress tensor describes the pressure exerted on a differential surface. T_{ij} is the pressure acting parallel to the i^{th} axis on a surface normal to the j^{th} axis. The diagonal elements correspond to the pressure acting in the normal direction to the surface and the off-diagonal elements correspond to the shear pressures acting in the tangential directions. To calculate the total force acting on a surface we can calculate the surface integral of the tensor as in (3.18).

$$F = \int T \cdot a_n \mathrm{d}s \tag{3.18}$$

(3.18) allows direct calculation of the force acting on the tip with the correct definition of $\boldsymbol{a_n}$ and d*s*. This technique was also used to calculate the volume of interaction by defining the $\boldsymbol{a_n}$ and d*s* to correspond to the surface of an equipotential volume in the sample.

To calculate the volume of sample material that was responsible for the total force acting on the tip, the equipotential surface that contains the material responsible for the majority of the force must be found. To accomplish this, the force is calculated using the Maxwell stress tensor at several equipotential surfaces within the material corresponding to

different depths. This data was then fitted to the curve found in (3.19). With the fit parameters β_1, β_2 & β_3 known the depth, x, corresponding to a fixed value, for example 90% of the total force, can be found by solving for x.

$$F = \beta_1\left(1 - \beta_2^{-\beta_3 x}\right) \tag{3.19}$$

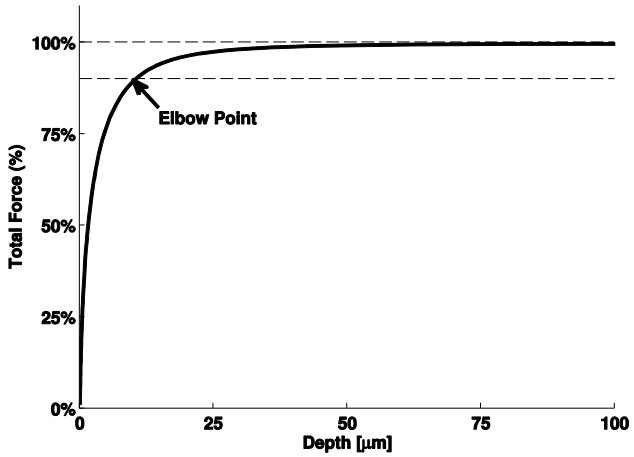


Figure 3.9: Plot of Force versus Depth for the equation of (3.19)

4 Results and Discussion

4.1 Experimental Data Analysis

4.1.1 Interpreting the Data

The output of the lock-in amplifier described in Chapter 2 was sent to the auxiliary analog input on the *NanoScope IIIa* controller. This input was recorded as a separate image channel along with height information gathered from the contact portion of the scan. To interpret the electrostatic response image recorded in Volts but representing the amplitude of vibration of the cantilever in meters, the lock-in settings must be recorded for each image and must not change during the capture process.

The relation between voltage from the deflection sensor and the displacement of the cantilever is approximately linear and changes with any adjustment of the deflection sensor, laser or cantilever and cannot be assumed from a previous setup. The first approach to characterizing this relation is a force plot (Figure 4.1). Here, the deflection of the cantilever is plotted against the extension of the piezo tube while engaging the tip against a hard sample. Prior to making contact with the surface, no deflection is recorded; this is seen as the horizontal segment in the force plot, A of Figure 4.1. As the tip approaches the surface, attractive van der Waals forces snap the tip into contact causing the small bump at point B. As the tip is pressed into the surface it deflects proportionally to the distance travelled by the piezo. The slope of this linear segment the the left of B (V/m) may be used to calibrate the deflection signal of the cantilever. As the tip is retracted, moisture present on the surface holds the tip until it snaps off the surface. The

force to disconnect the tip is larger than the van der Waals force and is responsible for point C.

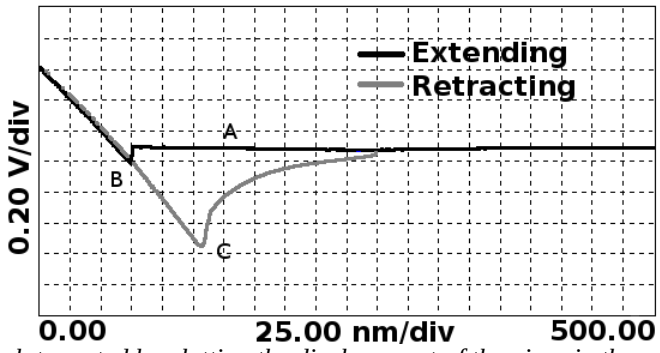


Figure 4.1: A force plot created by plotting the displacement of the piezo in the z direction versus the voltage representing vertical displacement of the cantilever. This plot was created by engaging the tip into the aluminum sample holder.

The problem with using the force plot to determine the relationship between voltage and distance is that it can be a destructive process. The tip may be damaged and the cantilever may be broken off the block, so this technique must be left until all measurements have been completed in order to safeguard the data collection process. To avoid these concerns, a thermal method can be used.

The thermal method assumes that a harmonic oscillator will oscillate due to the thermal energy present in the system; therefore the cantilever must be in thermal equilibrium with its environment [31]. This assumption cannot be met under vacuum as the heat dissipation is only radiative, therefore this procedure must be done in atmospheric conditions where there are also conduction and convection currents. Assuming thermal equilibrium, the energy associated with the ambient temperature will correspond primarily to the fundamental resonance frequency of the cantilever and all other modes can be ignored [31].

The thermal method equates the energy represented by the area of the resonance peak in the spectrum of the displacement signal with the thermal energy present in the environment to calculate the relationship between voltage and cantilever displacement, *x* in (4.1). To do this, the spectrum was captured using an SR760 spectrum analyzer connected via a serial cable to the computer running a custom downloading application. This spectrum is in units of V/√Hz and must be converted to units of Joules per 'frequency bin' before it can be manipulated. To do this, (4.1) was used, where *k* is the spring constant, *f* is the width of a single frequency bin in the spectrum and *x* is the relation to be determined.

$$\left(spectrum\left[\frac{V}{\sqrt{Hz}} \right] \cdot x\left[\frac{m}{V} \right] \right)^2 \cdot \frac{1}{2} k\left[\frac{N}{m} \right] \cdot f\left[\frac{Hz}{bin} \right] = spectrum\left[\frac{J}{bin} \right] \tag{4.1}$$

The relation between cantilever displacement and voltage was initially factored out and determined later. A cumulative sum of the scaled spectrum is plotted as in Figure 4.2, to determine the energy associated with the resonance peak, ΔE. This energy is due only to thermal oscillations and is equal to $k_B T$. The relation between displacement and deflection sensor output can now be found using (4.2).

$$\sqrt{\frac{\Delta E}{k_B T}} = x\left[\frac{m}{V} \right] \tag{4.2}$$

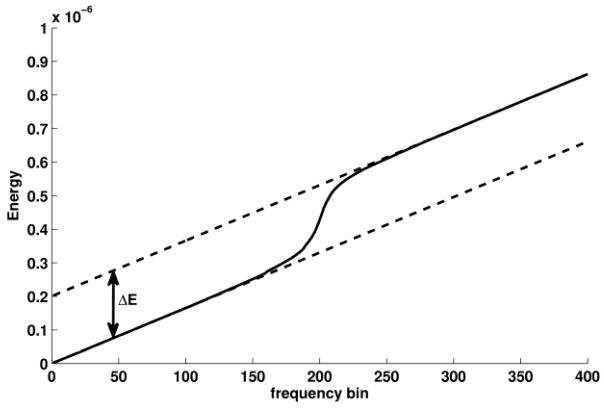


Figure 4.2: Cumulative sum of a scaled displacement spectrum. This data was collected using the NSC18 cantilever at room temperature and pressure.

With the relation between deflection amplitude and sensor output known and the spring constant, *k*, obtained from the data sheet, the output of the deflection sensor could then be used to measure force using (2.3). For the cantilevers used in these experiments (MikroMasch NSC18-Ti-Pt) the spring constant was typically 3.5 ± ~50% [N/m] [32].

The quality factor, *Q*, and resonant frequency were determined under the normal operating conditions. To measure this data, the EnviroScope chamber was pumped down to the desired pressure (approximately 10^{-1} as described in Section 2.3) and a displacement spectrum was again captured. The resonant frequency and bandwidth of this peak represents the resonant frequency and bandwidth of the cantilever while under vacuum.

Using the information gathered above, the captured data from the deflection sensor output was interpreted to the amplitude of vibration of the cantilever. The first step to doing this was to undo the amplification of the original signal due to the lock-in amplifier. The voltage signal at the input of the lock-in amplifier is related to its output

signal by [33]:

$$output = \left(\frac{input}{sensitivity} - offset \right) \cdot expand \cdot 10\text{V} \tag{4.3}$$

Where *sensitivity*, *offset* and *expand* are the settings of the lock-in amplifier that were recorded for each captured image. The input signal was found using this relationship and then converted to the amplitude of vibration of the cantilever in meters using (4.2).

To calculate the force acting on the tip, (2.3) derived in Chapter 2 was used. It is restated here:

$$A_v \approx \frac{Q}{k} \left| F_\Omega \right| \tag{2.3}$$

4.1.2 Data Collection

Several data sets were collected on three different samples, the TGZ-01, -02 & -03 manufactured by MikroMasch [34]. These samples are gratings designed to calibrate the z-axis of the piezoelectric positioning tube. The grating samples consist of a silicon substrate with a silicon dioxide layer grown on the surface to varying thicknesses (TGZ-01 = 20 nm, TGZ-02 = 100 nm & TGZ-03 = 500 nm) then etched with a square, 3 μm periodic pattern. The sample is then protected with a 10nm layer of Si_3N_4 to prevent oxidation of the exposed Si surface.

The grating samples were scanned at the minimum scan rate allowable by the software, 0.1 Hz. This was necessary to allow sufficient time above each data point for the

electrostatic response of the cantilever to stabilize. Above any given location on the surface, the cantilever amplitude of vibration changed in response to the local electrostatic force applied to it. The rate at which the amplitude of vibration changed is dependent on the quality factor of the cantilever which was on the order of 10^3 to 10^4. To ensure that the cantilever had sufficient time to stabilize, the time constant of the system was calculated. The second order differential equation describing the motion of a forced harmonic oscillator is [35]:

$$\frac{\partial^2 z}{\partial t^2} + \frac{\omega_0}{Q}\frac{\partial z}{\partial t} + \frac{kz}{m} = \frac{F}{m} \tag{4.4}$$

A solution to (4.4) decays with the factor of $e^{-t/\tau}$, where $\tau=2Q/\omega_0$ [36]. To ensure that the cantilever has settled above every given data point, it should remain above it for at least 3τ; this will enable the cantilever to settle to 95% of its final value. The MikroMasch NSC18-Ti-Pt tips used in this experiment have a typical resonant frequency of 75 kHz and under low vacuum had a quality factor less than 10^4 providing a time constant less than τ=42.4 [ms] [32]. The total time required per scan line was 16.3 seconds to scan 128 points across the sample surface allowing 3τ for each point.

The TGZ-02 sample grating was scanned the most extensively. This was done to verify the analytical model described in Chapter 3. This sample was scanned with a lift height of 150 – 500 nm at an interval of 25 nm with an amplitude of applied voltage of 1 – 4V at intervals of 1V. The TGZ-01 and TGZ-03 grating samples were scanned at an applied voltage of 3 and 4 Volts.

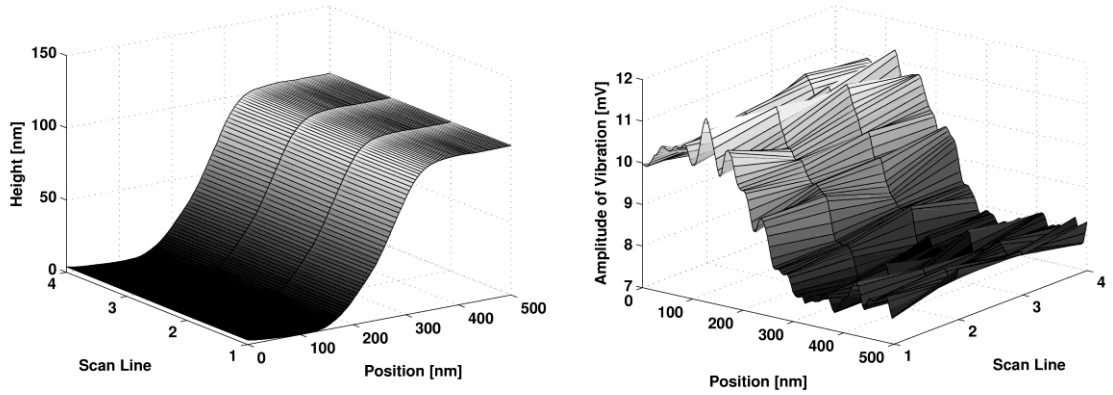


Figure 4.3: A typical scan of the TGZ-02 sample grating taken at a lift height of 300 nm and an applied voltage of 3V. The image on the left is height data and the image on the right is the electrostatic response of the tip.

Figure 4.3 is a representative set of scan data in which the electrical response appears inverted compared to the topographical image. This inversion is due to the lower permittivity of the SiO_2 as compared to the Si substrate. This inversion was predicted by the models presented in [37,38] and experimentally verified. The method outlined in [37] used a DC EFM technique to obtain a similar electrostatic response to those seen in Figure 4.3, obtained from the use of the heterodyned electrostatic technique discussed in Section 2.2. To analyze the scan data in a methodical manor, the data points were divided into two groups: the points above silicon and the points above silicon dioxide. This was accomplished using the height data; the midpoint of the smooth transition was found and 10% of the total width was ignored on both sides of the midpoint. The remaining 80% of the data points were then split into the two groups representing the electrostatic response of the tip over the Si substrate and over the SiO_2 steps. The mean and standard deviation above Si and SiO_2 were then calculated for all applied voltages and plotted versus lift height in Figure 4.4 & Figure 4.5.

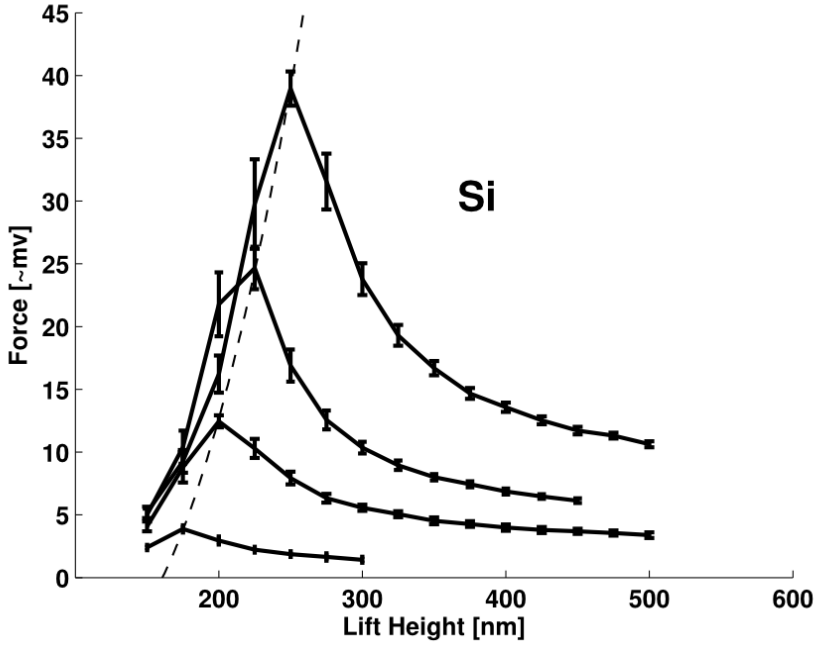


Figure 4.4: Amplitude of vibration of the cantilever (which is proportional to force) when above silicon versus cantilever lift height for applied voltage of 1 to 4 Volts.

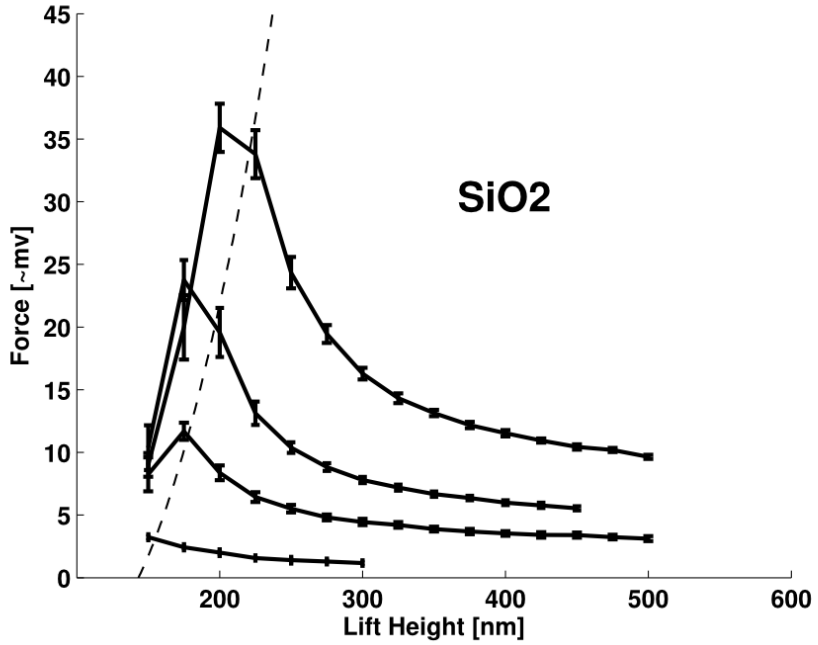


Figure 4.5: Amplitude of vibration of the cantilever when above silicon dioxide versus cantilever lift height for applied voltage of 1 to 4 Volts.

Figure 4.4 & Figure 4.5, suggest that the force seems to asymptotically approach zero. This is as expected; as the tip is withdrawn from the surface toward infinity, the polarization of the material decreases causing the force to tend to zero. Further, for every applied voltage there is a corresponding lift height that will yield a maximum response force, highlighted by the dashed lines through the force maxima in these figures. This maximum force does not occur at the same lift height for the Si and SiO_2 samples, so this defines an operational range between optimal lift heights when scanning these samples.

The ratio response, defined as the ratio of the force on the tip while above the SiO_2 step divided by the force on the tip while above the Si substrate, was calculated and plotted in Figure 4.6. This plot visually suggests two regimes: the near response and the far response. The near response occurs when the tip is close to the surface and is seen in Figure 4.6 as the section before the tails extend toward infinity. In this region the force attributed to the SiO_2 is greater than that due to the Si, an inversion that likely results from the interaction of the conical surface of the tip with the side wall of the SiO_2 step. This is discussed further in Section 5.3.

The far response is plotted in Figure 4.7 with the near response omitted. This is the expected response when considering the permittivity of the material. A small permittivity will permit less polarization and hence a smaller force will be seen by the tip, where as a large permittivity will permit more polarization causing a larger force to be observed.

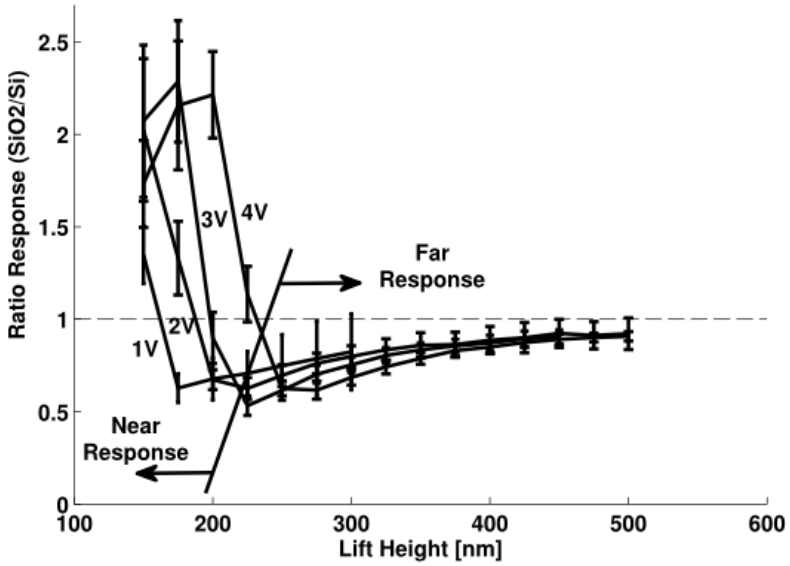


Figure 4.6: The ratio response for several voltages versus the lift height of the cantilever.

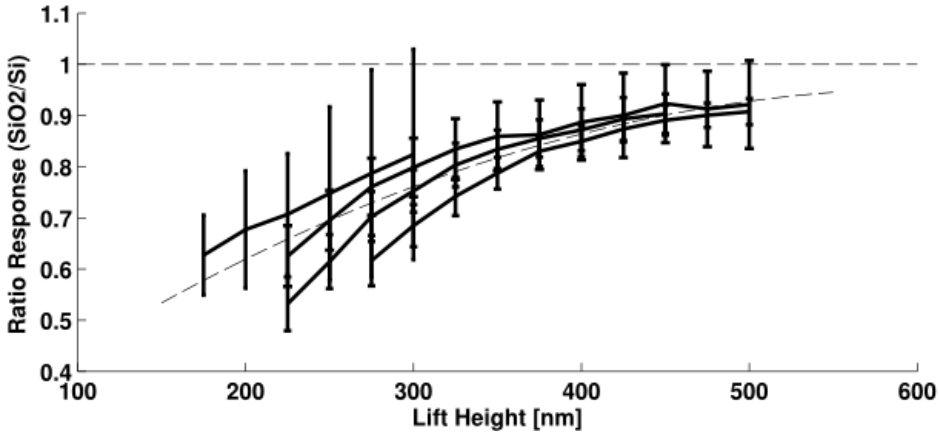


Figure 4.7: This is the subset of the data in Figure 4.6 representing the far response asymptotically approaching a ratio of one. The dashed line represents an average approach to unity.

4.2 Analytical Data Analysis

The data collected from the analytical model was used to verify that the model is accurate and to predict the volume of interaction. To verify the accuracy of the model, the same outputs were generated from the model that was gathered experimentally, specifically the

force acting on the tip.

Figure 4.8 & Figure 4.9 shows the plots of the data generated from the analytical model described in Chapter 3, it is the analogue of what is shown in Figure 4.4 & Figure 4.5, generated from the experimental data. From the comparison of these two data sets it is obvious that the analytical model does not account for the behaviour of the tip when in the near region. This result would be expected if the experimental data were not previously examined. This implies that there is something that the analytical model does not take into account that is occurring in the experimental data. Based on the *COMSOL* simulations presented in Chapter 5 it is proposed that the interaction of the tip with the side of the SiO_2 step was the cause of the inversion in the experimental data seen in Figure 4.3. This conclusion was drawn because the numerical simulations show this inversion when the tip was 50 nm from the boundary regardless of whether or not the cantilever was included in the simulations, whereas this behaviour was not seen when the tip was 750 nm away from the boundary (see Figure 5.8 in Chapter 5).

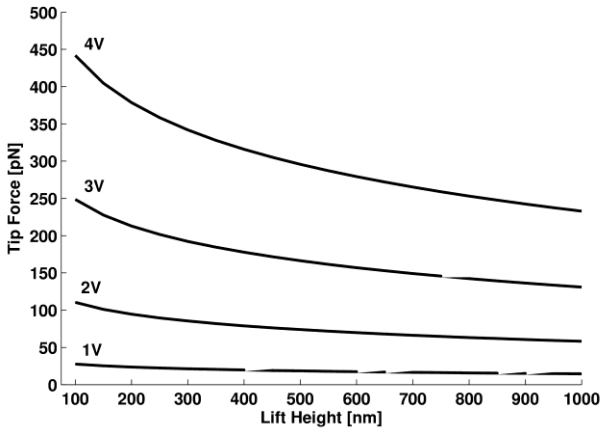


Figure 4.8: Force above Si calculated on the tip versus cantilever lift height for applied voltage of 1 to 4 Volts.

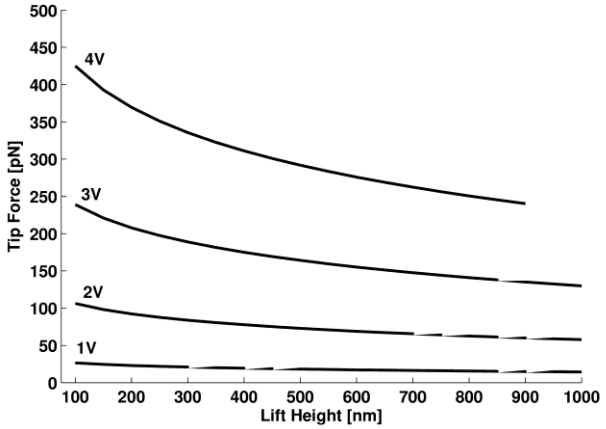


Figure 4.9: Force above SiO_2 calculated on the tip versus cantilever lift height for applied voltage of 1 to 4 Volts.

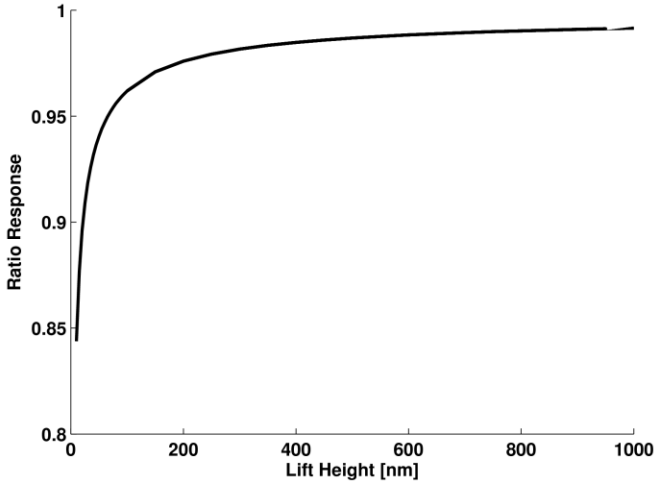


Figure 4.10: The ratio response calculated as a function of lift height

Figure 4.10 shows the ratio response generated from the analytical model, analogous to Figure 4.6. The analytical ratio response clearly resembles that obtained from the experimental data; however the steepness near the origin is greater. It is speculated that this difference is due to the simplification in the analytical model where the SiO_2 step is replaced with an infinite sheet of SiO_2 of the same thickness.

The data collected from the analytical model in the far region follows the form of the experimental data closely; this provides confidence that the calculated information regarding the volume of interaction and resolution is reasonable. To determine the volume of interaction, a region of the material was defined below the surface as a contour of constant voltage. This contour was very close to a sphere so the radius and centre point of a sphere were fitted to the contour; the centre point was always found to be near the tip of the probe. The force acting on the material was then found by calculating the Maxwell stress tensor over the surface of the intersection of the sphere with the material. To determine the volume responsible for the majority of the force acting on the cantilever, an iterative 'divide and conquer' process was employed. The two start points corresponded to an extremely small volume and an extremely large volume found by selecting a voltage at a small depth and a large depth into the surface. These two voltages defined two volumes of constant voltage that were used to find the corresponding forces acting on the material. The target force must be between the two extreme forces and was found by dividing the region between the two points into two sub regions and picking the region that contained the force, then iteratively splitting the region until the force was found to within an accuracy of 10^{-4} [N].

The target force was chosen to be 90% of the force acting on the cantilever. This decision was based on the plot in Figure 4.11; this shows that as the depth of the volume of constant voltage is increased, the percent of the total force acting on the cantilever ramps up quickly then asymptotically approaches unity. The elbow of the plot was a reasonable

choice for a threshold; this point occurs at approximately 90% of the total force.

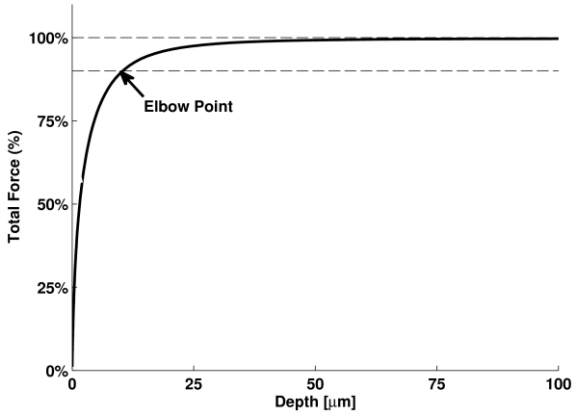


Figure 4.11: Total force (%) acting on the cantilever found by calculating the Maxwell stress tensor over a volume defined by the depth of its deepest point.

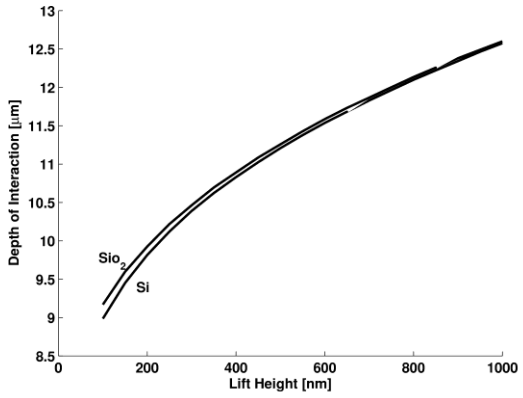


Figure 4.12: Depth of interaction volume versus lift height for a tip above SiO_2 and Si.

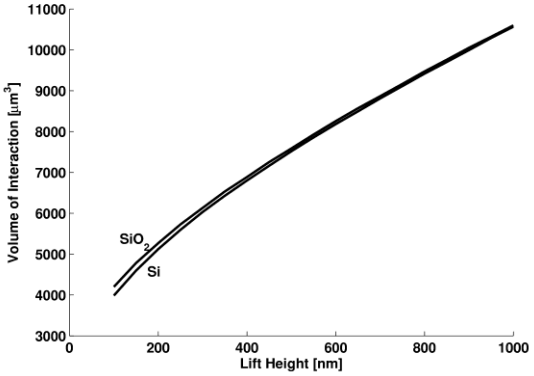


Figure 4.13: Interaction volume versus lift height for a tip above SiO_2 and Si.

The depth and volume of constant voltage was calculated at various lift heights, but is independent of applied voltage. The plots in Figure 4.12 & Figure 4.13 predicted that the depth and volume is dependent on the material, Si or SiO_2. As the lift height was increased past approximately 600 nm, the effects of the SiO_2 layer became negligible. This was due to the thickness of the SiO_2 sheet being three orders of magnitude thinner than the thickness of the Si substrate; as the tip is lifted above the surface, the fields in the

region are determined to a greater extent by the larger structures. Figure 4.12 represents the depth into the material from the surface that the contour of constant voltage takes, but because this contour is roughly spherical and the distance between the surface and the centre of the sphere is much less than the radius of the sphere, the depth also represents the lateral resolution of the technique. It suggests that this technique coupled with this sample will yield a poor lateral resolution in the range of tens of micrometers. This resolution is insufficient even for this micrometer scaled calibration grating sample.

4.2.1 Lateral Resolution

To show that the resolution found in the previous section is possible, a technique outlined by Gomez-Monivas et al. [39] was used to calculate the lateral resolution. This technique assumes that the dielectric thickness is small in comparison to a typical field gradient, an assumption that is not maintained in this case; this will show a completeness of investigation.

The technique outlined here is a perturbative approach to calculating the electric fields due to dielectric and topographic inhomogeneities placed on a homogenous substrate. (4.5) is the starting point for this method; it relates the homogenous electric field E_0, the capacitance C_0 and the applied voltage V to the electrostatic energy of the homogenous case U_0 [39] [40].

$$U_0 = \frac{1}{2}\int \varepsilon_0 E_0^2 dv = \frac{1}{2} C_0 V^2 \tag{4.5}$$

The electrostatic force of the homogenous case can be determined by finding the gradient

of the energy using (4.6).

$$F_z = \frac{-\partial U_{\mathbf{0}}}{\partial z} = -\frac{1}{2}\frac{\partial C_0}{\partial z}V^2 \tag{4.6}$$

To account for inhomogeneities the change in electrostatic energy is calculated as the volume integral of the polarization field ***P***, which is a function of the total field ***E***.

$$\Delta U = -\frac{1}{2}\int P \cdot E_{\mathbf{0}} dv = -\frac{1}{2}\int E\varepsilon_0\left(\varepsilon_r(r)-1\right)\cdot E_{\mathbf{0}} dv \tag{4.7}$$

As previously mentioned (Section 3.1), the total field $\boldsymbol{E_0}$, in the vicinity of the tip has no general analytic solution; Laplace's equation must be solved numerically in order to estimate a solution. Using a pertubative approach [40], the total field was replaced with the homogenous field and a correction factor that considers the discontinuous boundaries. This simplification is based on the assumption that the dielectric thickness is small in comparison to a typical field gradient i.e. the tangential electric field is insignificant to the end result.

$$\Delta U \approx -\frac{1}{2}\int \varepsilon_0\left(\varepsilon_r(r)-1\right)\left(\frac{E_{0z}^2}{\varepsilon(r)} + E_0^2\right)dv \tag{4.8}$$

where $\boldsymbol{E_{0\|}}$ is the unpertubated field tangential to the surface. This can be written in terms of an equivalent surface profile, $\boldsymbol{Z_{eff}}$.

$$\Delta U \ -\frac{1}{2}\varepsilon_0\int Z_{eff}\cdot E_{0z}^2 dS \tag{4.9}$$

This profile contains all the information about the changing dielectric permittivity and topography. The change in force can then be found by a two dimensional convolution between the equivalent surface profile and the response function of the microscope. The response function contains information about the specific tip being used as well as the

placement of the tip in relation to the sample. It is expressed as:

$$f = \frac{\partial \left| E_{0Z}^{2} \right|}{\partial Z} \Bigg|_{S} \tag{4.10}$$

where *S* is the surface of the homogenous sample surface. The response function of (4.10) is only a function of the homogenous electric field and the geometry of the tip; with this function known, the lateral resolution can be calculated.

To calculate the homogenous electric field, the equivalent charge method was used. A Si substrate 430 μm thick was placed above an infinite ground plane representing the Si substrate of the TGZ sample series. The charges were placed and calculated according to the discussion in Chapter 3. The lateral resolution was then calculated from the fields found using the ECM by measuring the 3 dB point of the response function, (4.10). A plot of this response function is shown in Figure 4.14 with the 3 dB point marked. A resolution of 228.4 nm was calculated based on a typical lift height of 300 nm and the dimensions of the NSC18 cantilever described in Chapter 2. A plot of resolution versus lift height is seen in Figure 4.15; the plot shows a linear relation between lift height and resolution.

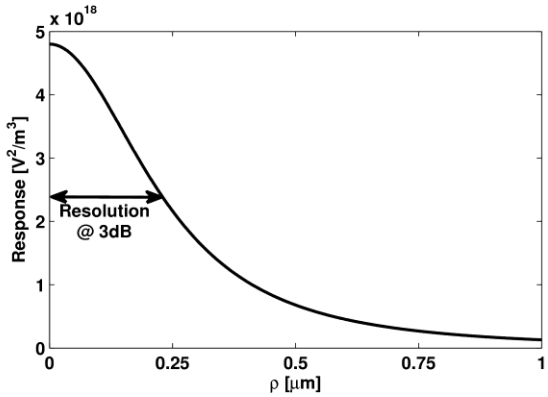


Figure 4.14: Response function of the NSC-18 cantilever tip at a lift height of 300 nm

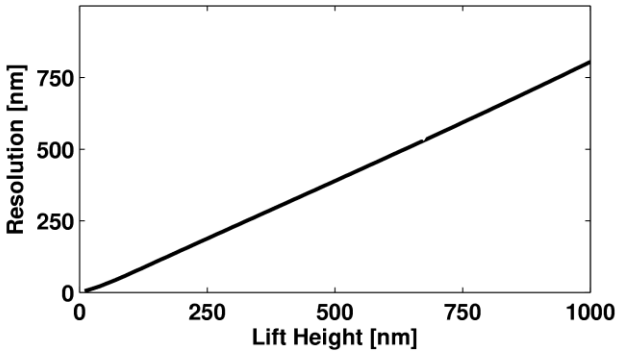


Figure 4.15: Predicted resolution versus lift height

The resolution determined from this technique was not in agreement with the numbers calculated from the analytical model. This is due to the failure of the TGZ sample to satisfy the assumption that the dielectric thickness is small in comparison to a typical field gradient. This suggests that this technique is best suited for samples of thin films formed over a conductive substrate.

4.2.2 Depth versus Relative Permittivity

Another use for the analytical model is to generate predictions of the depth or resolution as a function of the relative permittivity. This will provide insight into what type of

samples will provide suitable resolutions. To this end the analytical model was used to calculate the depth of interaction when the tip was 300 nm away from an infinite sheet of dielectric material 430 μm thick resting on a ground plane. The depth was calculated with the relative permittivity ranging from 4 to 1000 and plotted in Figure 4.16.

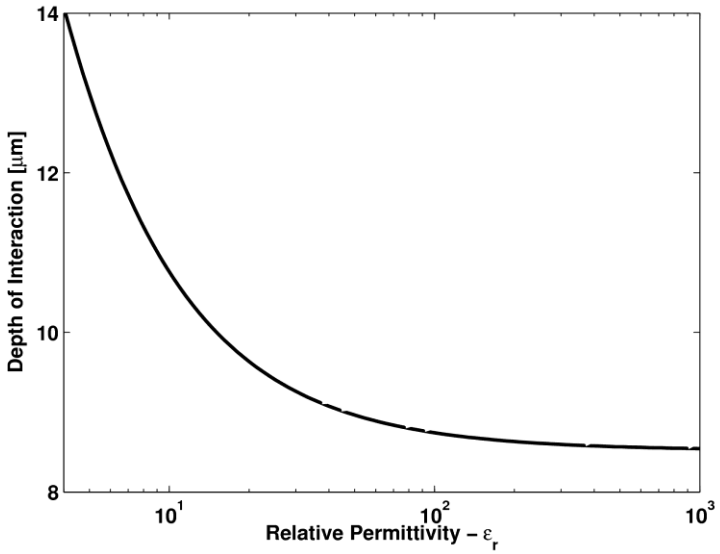


Figure 4.16: Depth of interaction plotted against the relative permittivity of an infinite dielectric sheet 430 μm thick resting on a ground plane with a tip-sample separation of 300 nm.

This plot shows a steep decline until a relative permittivity of ~100 is reached. This suggests that for this particular setup, a sample with a relative permittivity of approximately 100 will yield the best resolution, and in general the higher the permittivity of the material the better the resolution will be.

5 Numerical Electrostatic Modelling

5.1 Introduction to Finite Element Analysis and *COMSOL*

Finite element analysis is a numerical method used to find approximate solutions to partial differential equations over complex domains for which analytical techniques are either unsuited or prohibitively difficult to implement. The main advantage to the finite element method over other numerical techniques (such as the finite difference method) is that it is possible to vary the degree of accuracy for which different parts of a complex model may be solved, ie., with more detail at points of interest to the study and less detail elsewhere. This minimizes the computational power required to find a useful solution. Using this approach, a solution is estimated by discretizing the domain into *mesh elements* defined by a series of *nodes* and interpolating the values between the nodes on the element surface. To estimate the value at the nodes an expression is developed, that when minimized, will yield the desired solution. For the case of solving Laplace's equation, the potentials at the nodes are found such that they minimize the potential energy in the electric field, *W* [41].

$$W(V) = \frac{1}{2}\varepsilon_0 \int |\nabla V|^2 dV \tag{5.1}$$

To estimate the values at the nodes, the dependent variable *V(x,y)*, is approximated by a linear combination of known basis functions, φ_i multiplied by the unknown node values v_i [41,42].

$$V(x,y) = \sum_{i=1}^{N} v_i \varphi_i(x,y) \tag{5.2}$$

The number of nodes in the mesh, *N* will always be greater than the number of degrees of freedom because some of the nodes are defined by the boundary conditions of the problem statement. If there are *B* nodes defined by boundary conditions, then there are *N*-*B* degrees of freedom remaining to provide an estimate of the solution.

The approximation of (5.2) can then be substituted into the equation to be minimized, *W*. In the case of Laplace's equation, the potential energy is minimized with respect to the node voltages v_i. This yields *N*-*B* equations with *N*-*B* unknowns [41].

$$\frac{\partial W}{\partial v_i} = 0, i = 1..N - B \tag{5.3}$$

COMSOL Multiphysics [42] uses this simplistic principal and expands it to apply to a multitude of physical problems including heat transfer, structural mechanics and electromagnetics. *COMSOL* can employ several modules to solve complex problems, for example the structural dynamics module can be used with the electrostatic module to predict the elastic compression and expansion of a cantilever due to an electrostatic force. The simulations can be run in 1, 2 & 3 dimensional space as well as 1 & 2 dimensional modes that expand to 2 & 3 dimensional space based on rotational symmetry. This provided a powerful simulation tool to independently verify the model presented in this thesis.

5.2 Verification of Analytic Model

COMSOL was used to verify the mathematical model presented in Chapter 3, ensuring that the field calculations were correct. To this end, a specific geometric arrangement was

chosen; a tip voltage of 3 Volts, a lift height of 300 nm and a tip geometry corresponding to the NSC18 cantilever probe and the TGZ-02 sample grating (as assumed by the analytical model).

To begin simulating the analytical model, a two dimensional electrostatic axial symmetric model was selected, consistent with the symmetry assumed by the analytical model. The nature of an axial symmetric model suggests that all objects in the model are rotated about the vertical axis, therefore a point charge in a two dimensional axial symmetric model represents a circular line charge in three dimensions with a total charge of $Q=q_0 2\pi r$ Coulombs, where r is the distance from the axis of rotation and q_0 is the charge per unit length. If the point charge is located on the vertical axis, then r will be zero, therefore the total charge will be zero. To avoid this problem the point charges were located 100 pm from the vertical axis. The vertical position and magnitude of the point charges were determined from the analytical model and the magnitude of the charge was found using the previous relation, $q_0=Q/2\pi r$, where Q is the charge associated with one of the ten point charges used in the model.

Next, three sub-regions were added, one for the air above the sample, one for the SiO_2 sheet and one for the Si substrate (see Figure 5.1). These sub-regions are finite in extent (200 μm from the simulated tip) as *COMSOL* is unable to simulate an infinitely large region of space. The size of these regions was chosen to simulate a ground potential at infinity without the requirement for unreasonable amounts of memory and processing power. The relative permittivities for the three regions were adjusted to be 12, 4 and 1

representing Si, SiO_2 and air respectively. The boundary conditions were initialized and then a mesh made up of 700 thousand mesh elements was created and solved for 1.4 million degrees of freedom. The solution is plotted in Figure 5.1.

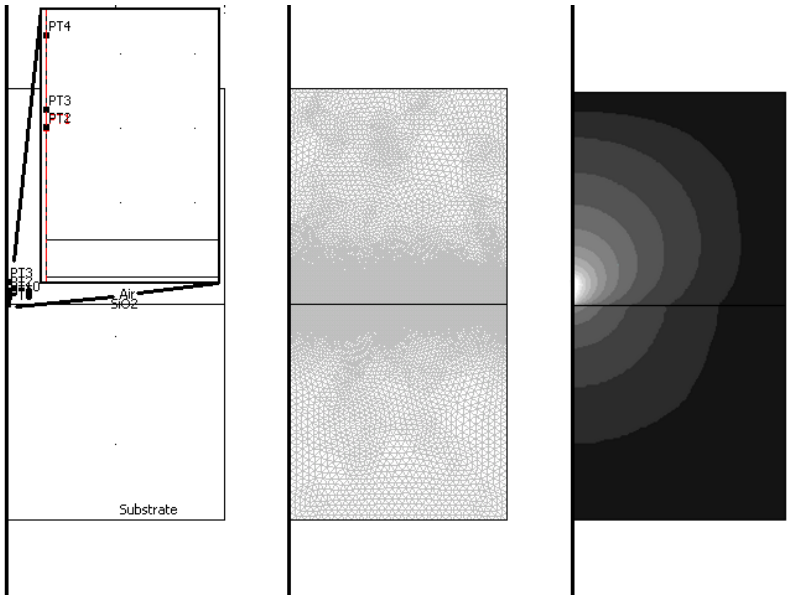


Figure 5.1: Left: The schematic representation of the analytical model in COMSOL; Middle: The mesh used to solve this model; Right: The voltage plot of the solution.

With the *COMSOL* numerical model solved, point values were compared with the analytical model. To this end, two lines were considered; the first was the line along the surface of the tip corresponding to the test points outlined in Chapter 3, and the second was a 700 nm vertical line, 500 nm from the axis of symmetry centred vertically about the SiO_2 layer (see Figure 5.2). Each line consisted of 100 points; for the tip surface the points were spaced biquadratically and for the vertical line the points were spaced linearly.

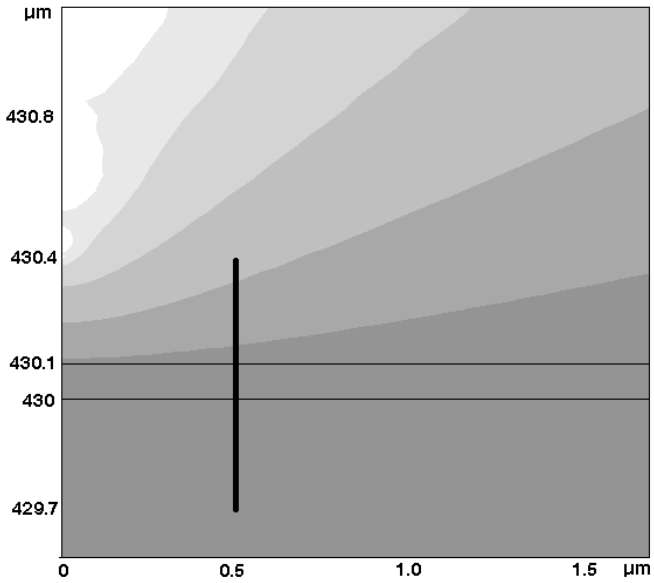


Figure 5.2: COMSOL solution focused on the voltage near the tip. The vertical line represents the region where the comparison was made.

Figure 5.3 shows the plot of voltage versus displacement for the vertical line of comparison. From the plot, it is clear that the *COMSOL* data is nearly the same as the analytical data. To obtain a measure of similarity a percentage difference was calculated, defined as the absolute difference between the two equivalent values divided by their average value. Two values that are the same would have a percentage difference of 0% where as a pair of extremely dissimilar values would yield a value greater than 100%. The percentage difference was calculated for every point along the vertical line and the RMS value was then found to be 2.93%.

Figure 5.4 shows the voltage along the surface of the tip as calculated both by *COMSOL* and the analytical model. The oscillating nature of this plot is due to the limited number of point charges. Using many more point charges would reduce this oscillatory behaviour significantly. The percentage difference was calculated at every test point along the tip surface and the RMS value for this data series was found to be 0.57%.

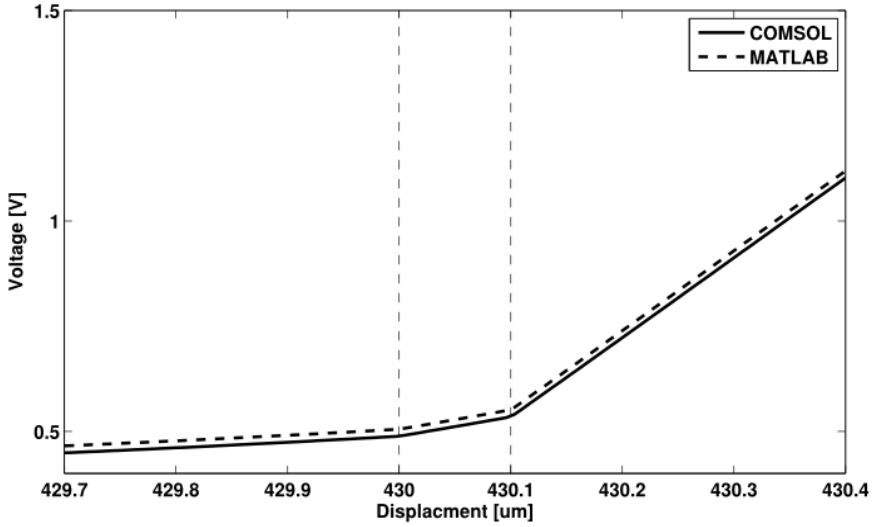


Figure 5.3: Comparison of COMSOL results to the analytical model along the vertical line crossing the SiO_2 layer.

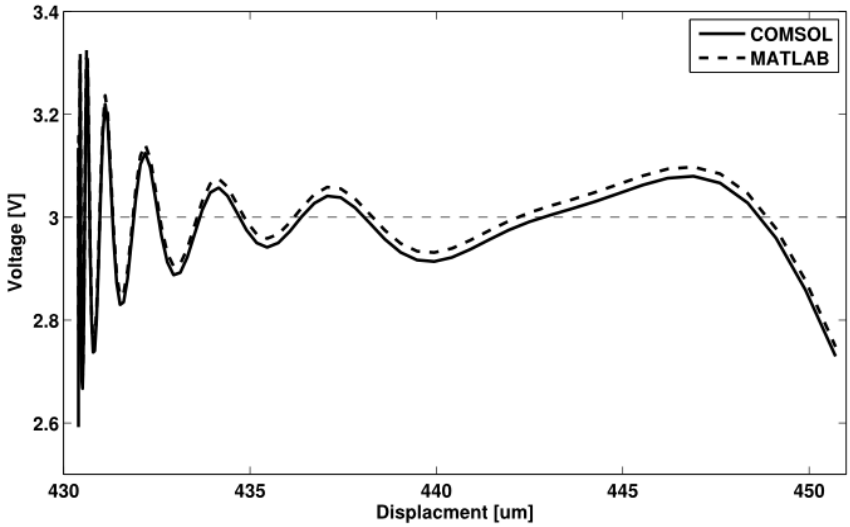


Figure 5.4: Comparison of COMSOL results to the analytical model at the test points along the surface of the tip.

From these results, it was concluded that the analytical model accurately represented the fields present around a series of point charges distributed along the vertical axis. Next, the analytical model was compared with a *COMSOL* simulation where the point charges

were replaced with a triangle, representing a conical tip when revolved about the vertical axis. This was done to explore how well the point charges approximated the fields around the conical tip. The surface of the tip was held at a potential of 3V. The remainder of the simulation was unchanged from the previous case (see Figure 5.5). This simulation was compared against the analytical model with 40 point charges, the same number of point charges that was used when computing the results of Section 4.2. The *COMSOL* simulation was then meshed with 713 thousand mesh elements and solved for 1.4 million degrees of freedom.

To gauge the similarity of the models, the same two lines of comparison were used. The RMS value of the percentage difference calculated along the tip surface was 3.86%. The RMS value of the percentage difference calculated along the vertical line of comparison was found to be 5.94%.

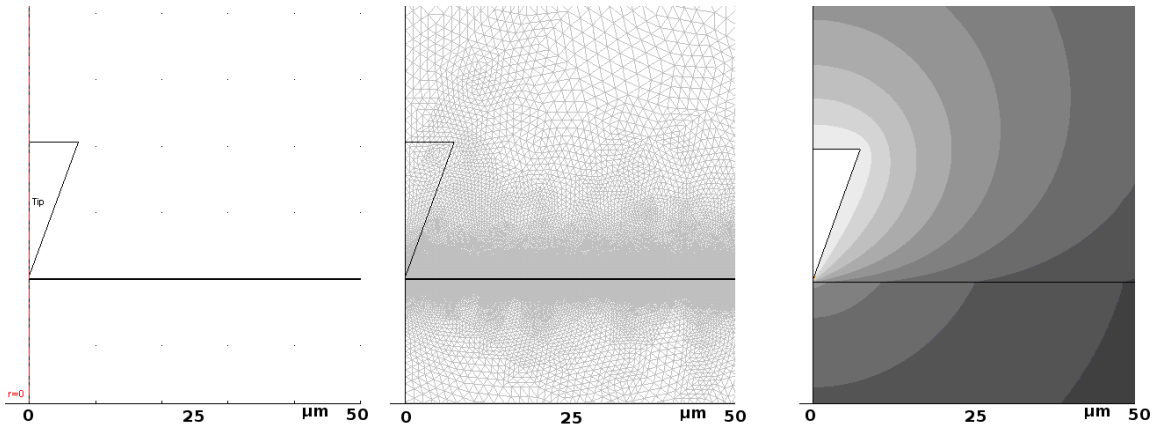


Figure 5.5: Left: Schematic depiction of the substitution of point charges with a triangular tip shape. Middle: The mesh used to solve this model. Right: The voltage plot of the solution.

5.3 Determination of Ratio Inversion

Figure 4.6 of Chapter 4 shows a plot of the ratio response versus lift height for several voltages and they all exhibit an unexpected inversion in the *near* region. To explore the cause of this inversion a further *COMSOL* simulation was undertaken. It was speculated that this inversion was due to either the presence of the cantilever or the interaction of the tip with the side of the SiO_2 step. To test these two hypotheses, a series of *COMSOL* simulations were conducted. The model consisted of a 200 μm cube to represent the Si substrate, a 200 μm cube to represent the air and a 1.5 μm x 24 μm x 100 nm block was placed on the centre of the Si surface to represent the SiO_2 (see Figure 5.6). The SiO_2 block was truncated at 24 μm to reduce the number of mesh elements required to solve the problem. The 100 nm dimension restricted the size of mesh elements that *COMSOL* could generate, producing a prohibitively large number of mesh elements. The length of 24 μm was chosen based on another series of simulation. The force on the tip was calculated as the SiO_2 step was increased from a 1.5 x 1.5 μm square until the force on the tip approached its asymptote. This provided assurance that a 24 μm SiO_2 step was sufficiently long to preserve the expected behaviour.

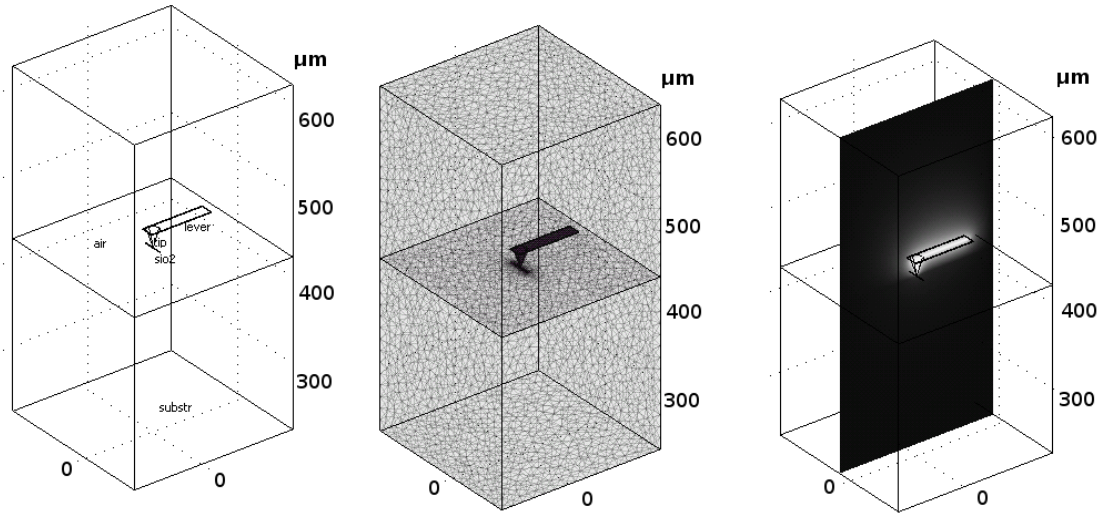


Figure 5.6: Left: Schematic depiction of the tip with cantilever. Middle: The mesh used to solve the model. Right: The voltage plot of the solution.

Two varieties of probes were used, first a tip without a cantilever was used by adding a cone above the SiO_2 step while the second type had this same cone with a block added above it to represent the cantilever (see Figure 5.6). These two tips were placed above the SiO_2 step at its centre, 750 nm from its edge and 50 nm from its edge, as well as above the Si, 50 nm from the step and 750 nm from the step (see Figure 5.7). A distance of 50 nm was chosen because it was a round number greater than the distance required to prevent contact between the tip and the surface, 36.4 nm, and a distance of 750 nm was chosen because it was the midpoint between the two edges of the SiO_2 step. These positions ensure that the tip will have little chance to interact with the side of the SiO_2 step when it is far from the step and great opportunity to interact with the side when they are near without contacting the edge with the side of the tip. These two tips were placed from 10 nm to 500 nm above the four positions with a tip voltage of 3V, because the ratio response is not dependent on the applied voltage. Each case of the model was then meshed with ~10^5 mesh elements and solved for ~10^6 degrees of freedom.

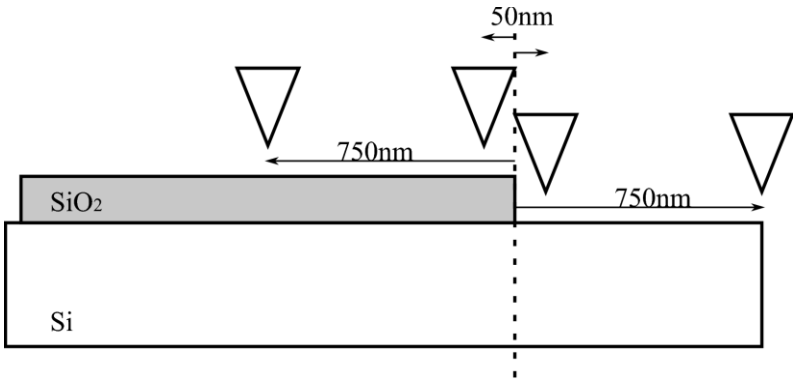


Figure 5.7: The four positions of the tip used to determine the nature of the ratio inversion.

Once each model was solved the force was calculated on the tip by integrating the Maxwell's stress tensor over the surface of the probe. With these values, the *near* ratio response was calculated by dividing the force above the SiO_2 step by the force above Si, 50 nm from the step edge. The *far* ratio response was calculated the same way using the forces 750 nm from the step edge. This was repeated for both probes, the conical tip with and without the cantilever. The results of these simulations are shown in Figure 5.8.

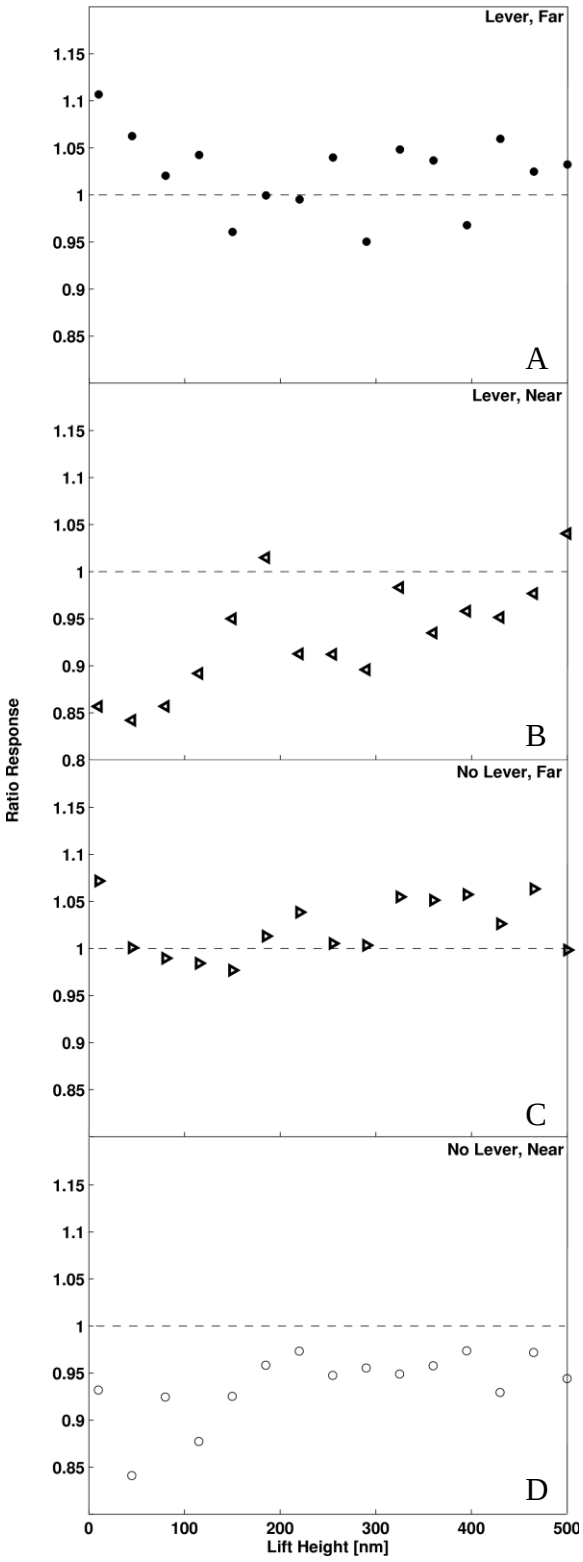


Figure 5.8: Far response and near response with and without the cantilever included in the model.

The data presented in Figure 5.8 is somewhat inconclusive. The scatter in the output from COMSOL arises from the low mesh density that was employed to calculate the Maxwell stress tensor. Higher mesh densities could be employed in these calculations, however the additional time per calculation and computational power required to improve the data scatter was not available. The data clearly shows two varieties of response. The first type, seen in Figure 5.8A & C, shows the response approaching unity from above whereas the second type, seen in Figure 5.8B & D shows the response approaching unity from below. This similarity between Figure 5.8A & C and Figure 5.8B & D suggest that the presence or absence of the cantilever does not affect the outcome of the calculation. As a consequence, it is reasonable to conclude that the inversion of the ratio response seen in the experimental data (and not seen in the analytical model) is due to the tip interacting with the side wall of the SiO_2 step.

5.4 Scan Line over SiO_2 Step

A *COMSOL* simulation was designed to produce a plot of the force acting on the probe versus the position of the tip over the surface by recreating a single scan line of the plot found in Figure 4.3. Once the *COMSOL* model was verified against the experimental data, the interaction depth and volume were calculated and compared to the analytical model.

The *COMSOL* model used to generate this information was very similar to the model used in the previous section to determine the cause of the ratio inversion. It too was composed of a 200 μm cube representing the Si substrate, a 200 μm cube representing the

air and a 1.5 μm x 24 μm x 100 nm block representing the SiO_2 step. The tip was simulated with a cone of the same height and radius as the NSC18 probe (see Figure 5.9A). The model was evaluated several times as the tip was scanned across the edge of the SiO_2 step (see Figure 5.9B). In each tip position the model was meshed to contain on the order of 200 thousand mesh elements and solved for approximately 350 thousand degrees of freedom. This is a fairly low mesh density for a three dimensional model with such a large ratio of dimensions; the result is a noisy solution (as seen in Figure 5.11).

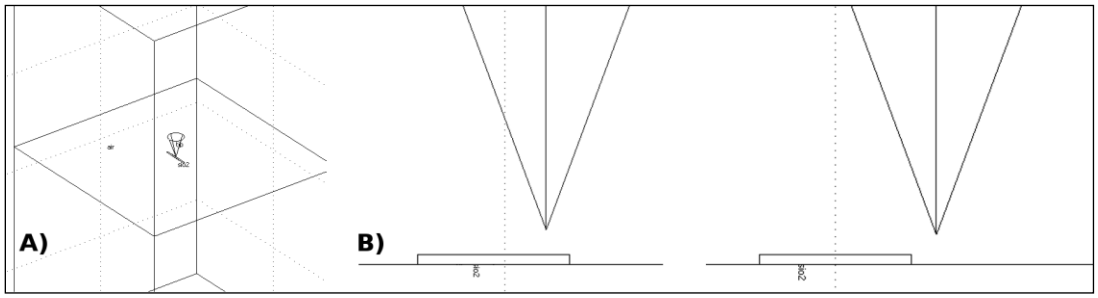


Figure 5.9: A) Schematic view of the tip over the sample surface in the COMSOL simulation environment. B) Enlarged view of the tip-sample region as the tip is scanned from left to right.

To aid in analysis, the noisy data was fitted to a logistic function of the form:

$$f(x) = a + \frac{b-a}{1+e^{-(x-x_0)/\tau}} \tag{5.4}$$

The shape of this model is seen in Figure 5.10; it contains four parameters: a and b are initial and final magnitudes, x_0 is the midpoint between these two magnitudes and occurs at the centre of the transition period, and τ represents the width of this transition period. The width of the transition band can be quantified by measuring the transition half width at 3τ defined as the horizontal distance between the centre of the transition period to the point where the magnitude is 95% of its final value plus 5% of its initial value. At these points, the model evaluates to:

$$f\left(x_0+3\tau\right)=a+\frac{b-a}{1+e^{-3}}\approx a(0.05)+b(0.95) \tag{5.5}$$

$$f\left(x_0-3\tau\right)=a+\frac{b-a}{1+e^{+3}}\approx a(0.95)+b(0.05)$$

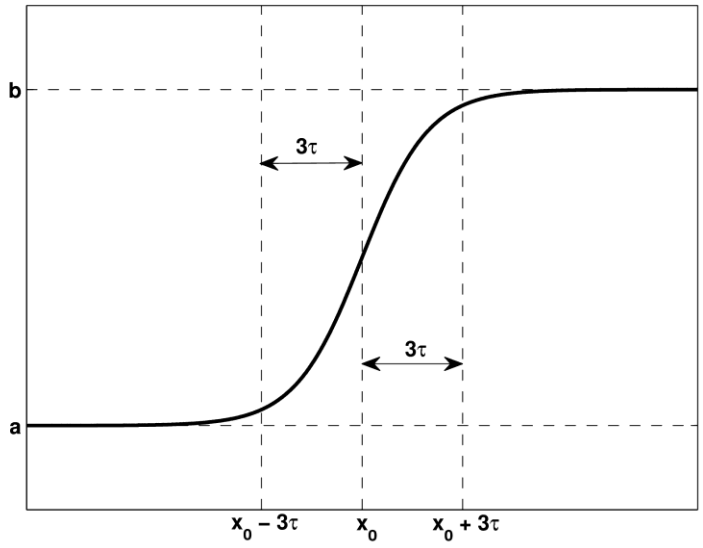


Figure 5.10:Graphical representation of the model fitted to the data sets. The parameters include a, b, x_0 and τ.

The data was collected from the *COMSOL* simulations by integrating the Maxwell stress tensor over the surface of the tip to calculate the force acting on the probe in each position above the sample. The data seen in Figure 5.11 shows the calculated force with a large degree of scatter. This scatter is due to the calculation of the Maxwell stress tensor; it is extremely sensitive to mesh density and as previously stated the mesh density for this series of computations was relatively low. The simulated force was then compared to the amplitude of vibration of the cantilever from the experimental data in Figure 5.11. To compare the similarity of the data sets, both the *COMSOL* data and the experimental data were fit to the logistic function (5.4) and plotted (with normalized magnitudes) in Figure

5.12. All four parameters of (5.4) were fitted to the two data sets and given in Table 5.1. The relatively poor fit coefficient for the *COMSOL* data reflects the high degree of scatter introduced from the calculation of the Maxwell stress tensor.

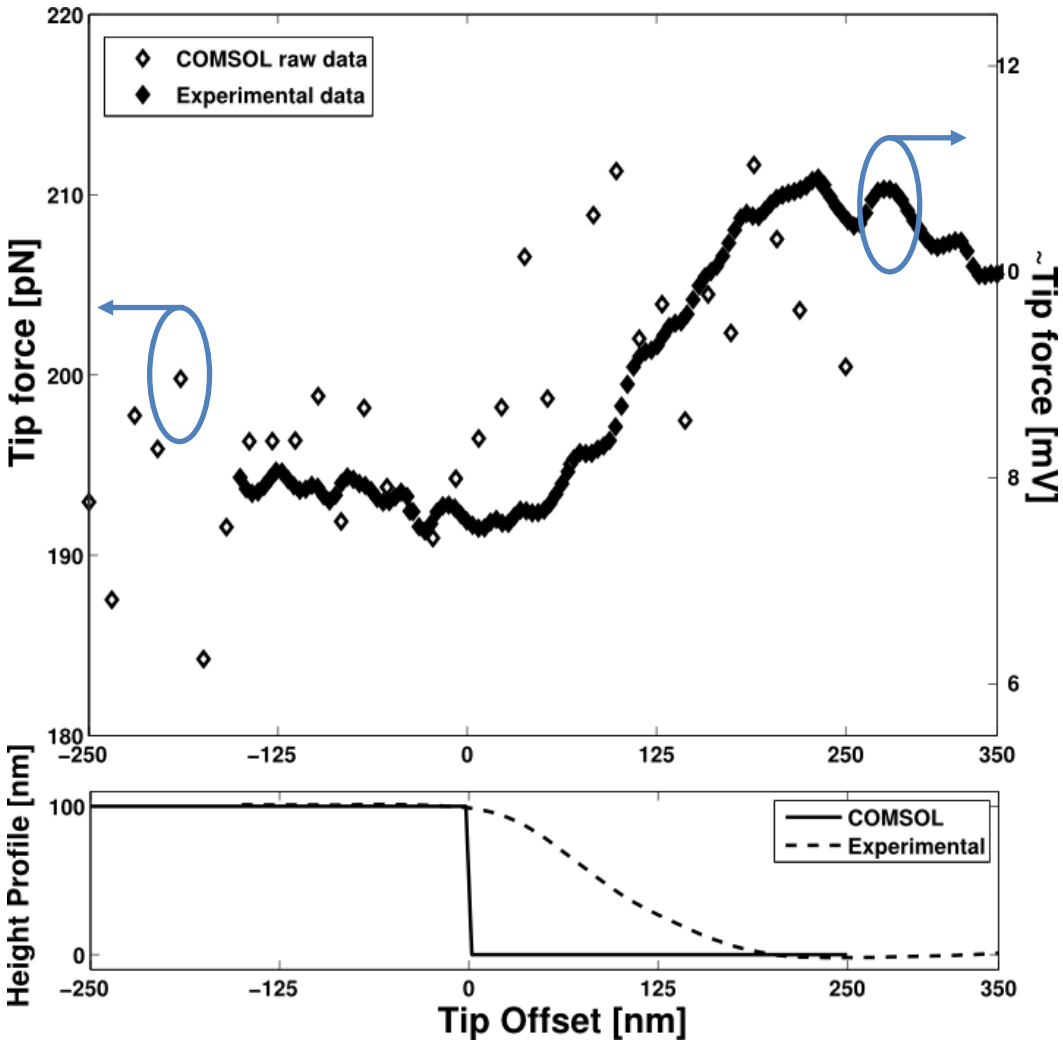


Figure 5.11: The force calculated by COMSOL acting on the tip versus the offset from the step edge forms the sparse data while the experimental amplitude of vibration, which is proportional to force acting on the tip versus the offset from the step edge forms the solid line. The COMSOL data is represented by the left vertical axis and the experimental data is represented by the right vertical axis. The relation to the surface profile is shown on the lower plot for both COMSOL and the experimental data.

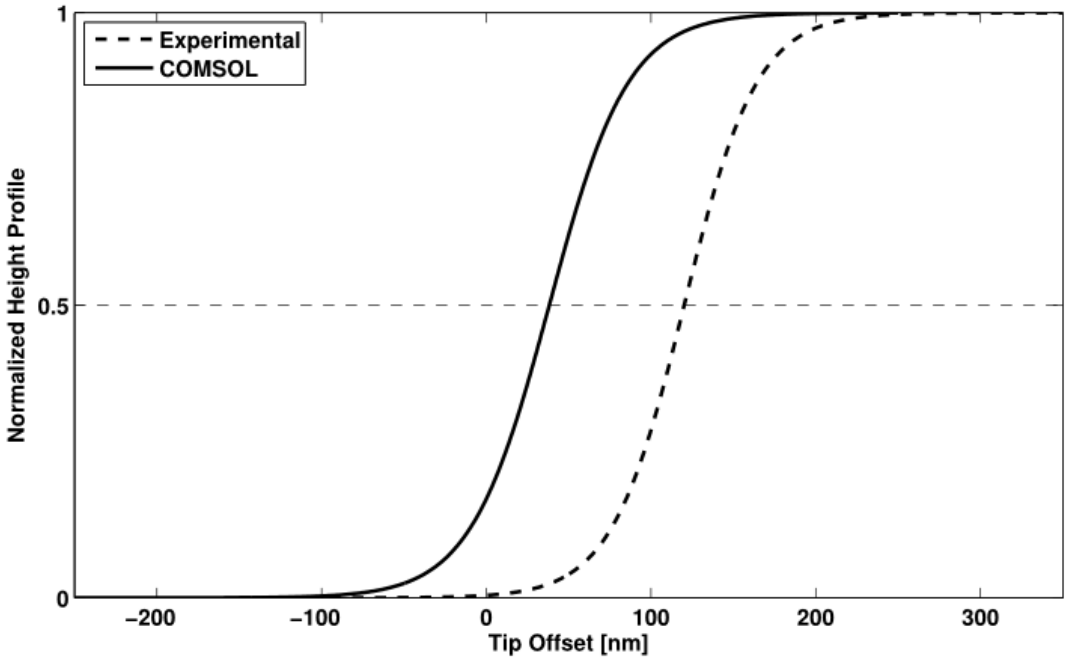


Figure 5.12: The Logistic function fit to the experimental data and the COMSOL simulated data.

Table 5.1: Fit parameters for the COMSOL simulations and experimental data.

	a	b	x_0	τ	R^2 *coeff.*
COMSOL	194 pN	206 pN	38.2 nm	24.0 nm	0.583
Experimental	7.77 mV	10.52 mV	120.1 nm	22.1 nm	0.972

In the comparison between the two data sets the magnitudes (parameters a and b) are ignored as the units of each set are dissimilar. This leaves the width and position of the transition period for comparison. It is evident from Figure 5.12 and Table 5.1 that the transition widths for both sets of data are fairly similar. The difference of this width will be compared using the half width, 3τ (see Figure 5.10). The experimental data has a transition half width of 3τ=66.33 nm and the *COMSOL* data set has a transition half width of 3τ=72.0 nm. These values have a percentage difference (absolute difference divided by

average value) of 8.2% or quite similar.

The position of the transition period is expected to be at $x=0$ if the discontinuity was only due to dielectric change as opposed to surface displacement as well. The discontinuity has been shifted to the positive end, away from the edge of the dielectric step. The *COMSOL* data was shifted by x_0=38.2 nm where as the experimental data was shifted by x_0=120.1 nm.

Because the experimental data and *COMSOL* simulation showed good agreement, information regarding the depth and volume of interaction was extracted from the *COMSOL* simulation. Figure 5.13 & Figure 5.14 show the depth and volume of interaction plotted against the offset of the tip from the edge of the SiO_2 step with a plot of the data fitted to (5.4). The analytical model in Chapter 4 (see Figure 4.12) predicted that the expected depth of interaction when above SiO_2 was 10.46 μm and when above Si was 10.39 μm. The plot of Figure 5.13 shows similar behaviour but suggests that the median depth of interaction above SiO_2 was 8.61 μm and the median depth above Si was 6.94 μm. This difference was due to two sources of error: first the noise associated with the meshing process in the finite element analysis (especially the calculation of the Maxwell stress tensor as it is very dependent on mesh size), and second, the simplification of the analytical model where the SiO_2 step was replaced by an infinite sheet of constant thickness.

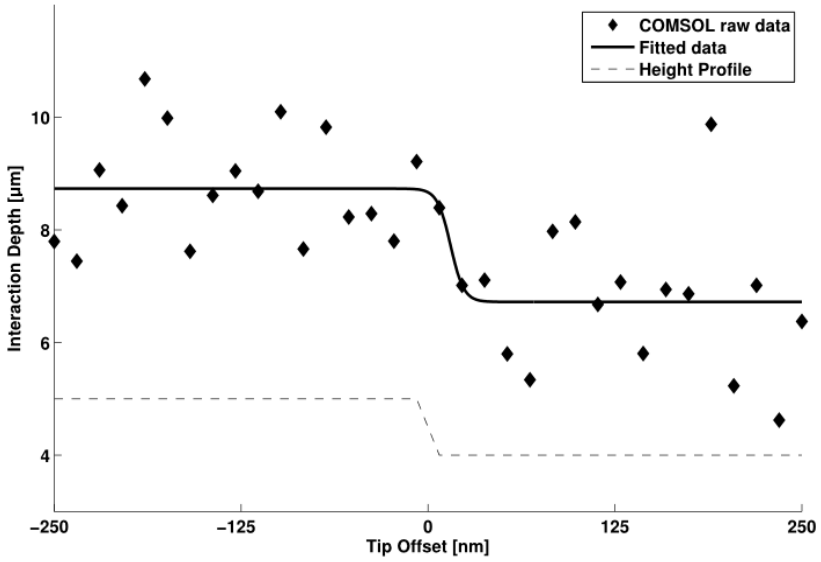


Figure 5.13:Depth of interaction plotted against the offset of the tip from the SiO_2 step edge. The solid line represents the data fitted to (5.4) and the dashed line represents the surface profile.

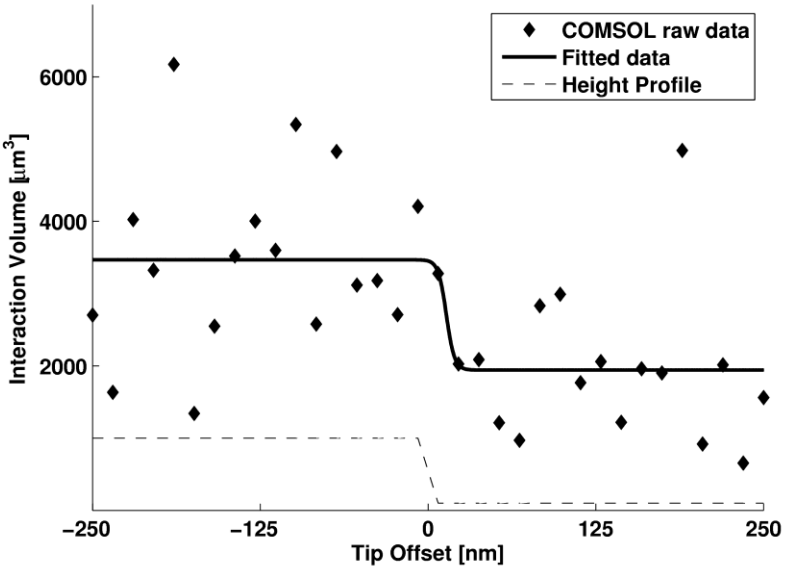


Figure 5.14:Volume of interaction plotted against the offset of the tip from the SiO_2 step edge. The solid line represents the data fitted to (5.4) and the dashed line represents the surface profile.

6 Conclusions

Chapter 3 outlines an electrostatic model that was used to predict the fields around an EFM tip and a TGZ series grating sample. The model makes use of the equivalent charge model to replace the complex surface of the tip with a series of point charges placed on the vertical axis. Within the model, the TGZ sample grating is represented by an infinite sheet of Si, 430 μm thick, resting on a ground plane with a 100 nm infinite sheet of SiO_2 resting on its surface. These simplifications allow the calculation of the force acting on the tip, the spatial resolution of the imaging probes and the volume of sample material that is interacting with the tip.

The model was implemented as defined within MATLAB and verified against a finite element simulation. The model and the FEM simulations are in good agreement. The RMS percentage difference between the analytical model and the FEM simulation was 0.57% on the surface of the tip and 2.93% along a line of comparison 500 nm from the axis of symmetry. These results demonstrate good agreement between the analytical model and the fields predicted by electrostatic theory due to localized point charges. Next the model was compared with an FEM simulation of a conical conducting tip above a simulated sample surface. The RMS percentage difference between the analytical model and the FEM simulation was calculated as 3.86% along the surface of the tip and 5.94% along the line of comparison. These values are slightly larger than the previous case because the simulations are not modelling exactly the same setup. In the first case, a series of point charges was being compared to a series of point charges but in the second

case, a series of point charges was being compared to a solid conical tip. As such a 5% difference is acceptable.

With the model accurately predicting the fields around the tip and sample, it was then programmed to simulate the experimental setup. The TGZ-02 sample was modelled and the force acting on the tip under various lift heights and applied voltages was then calculated. The shape of the force plots above Si and above SiO_2 (see Figure 4.8 & Figure 4.9) was compared with the shape of the plot of amplitude of vibration obtained from the cantilever during the experimental work. This comparison found some differences in the behaviour of the experimental and analytical results but generally predicted the same shape that was observed in the experimental work.

The major difference between the experimental and analytical data was found in the ratio of the response, (force), i.e. the ratio of the force above the SiO_2 step and the force above the Si substrate. The experimental data showed an inversion in this ratio when the tip was near the surface but this inversion was not seen in the analytical model. It was suggested (Section 5.3) that this inversion was due to additional electrostatic interactions between the side wall of the SiO_2 step and the edge of the tip. The analytical model could not predict these forces because it replaced the SiO_2 step with an infinite sheet of the same thickness so there was no side wall present.

As the analytical model produced similar results to the experimental data, it was used to extract an estimation of the volume of interaction and the spatial resolution of the

technique. Figure 4.12 & Figure 4.13 presented plots of interaction depth and volume. These plots show us that at a lift height of 300 nm the depth of interaction (which provides an estimate of the lateral resolution as well) was on the order of 10 μm and the volume of interaction was on the order of 6000 μm^3. A lateral resolution of 10 μm is quite poor and could account for the soft sloping electrostatic response found in Figure 4.3. The model was also used to predict the variation of depth or resolution with permittivity. The model suggested that a low permittivity was detrimental to resolution; a relative permittivity of 4 (as SiO_2) would increase the minimum resolution from approximately 10 μm to 14 μm. An increase in relative permittivity from 12 to 100 had the effect of lowering the resolution from 10 μm to approximately 9 μm and an increase in relative permittivity from 100 to 1000 had very little effect on the resolution.

With the insight gained from the application of the analytical model described in this document an important piece of knowledge was gained: this EFM technique works best with thin coverage over a conducting ground plane as the resolution increases with decreasing thickness. This has implications for sample choice and preparation; thin film samples on the order of hundreds of nanometres thick will provide the best spatial resolution.

6.1 Future Work

To improve upon the work presented in this thesis, the most important place for improvement is the electrostatic model presented in chapter 3. A major simplification was made to aid in the development of the model. This simplification was the substitution of

an SiO_2 step on top of an Si substrate with an infinite sheet of Si representing the substrate and an infinite sheet of SiO_2 representing the step. This simplification enabled the use of the equivalent charge method which requires rotation symmetry. A logical improvement would be to find a method to model the step while still predicting the fields of the tip with reasonable accuracy.

Another area of improvement is the equivalent charge method. The charge required to build the fields in the vicinity of the tip-material interface does not ensure the fields surrounding the tip in the vicinity of the cantilever are correct. This was not possible using the ECM, instead the ECM had a larger than normal field in the region above the tip and may have skewed the data by decreasing the force acting on the tip.

A final area of improvement would be to enable time dependent modeling of the dynamic heterodyned technique. This model has assumed a worst case deflection approach instead of modeling the dynamic behaviour of the cantilever under forced oscillation. This may improve the consistency of the model with the experimental data.

With these improvements the electrostatic model would be able to produce scan lines that show the deflection of the cantilever as it is traced across the surface of the simulated sample as well as provide a better estimate of the experimental technique.

7 References

[1] M. E. Barrow, "The Development of the Microscope," *Bios*, vol. 5, no. 4, pp. 157-161, Dec. 1934.

[2] E. Abbe, *Archiv für mikroskopische Anatomie*, vol. 9, pp. 413-480, 1873.

[3] E. H. Synge, "A Suggested Method for extending Microscopic Resolution into the Ultra-Microscopic Region," *Philosophical Magazine*, vol. 6, pp. 356-362, May 1928.

[4] E. H. Synge, "An Application of Piezo-electricity to Microscopy," *Philosophical Magazine*, vol. 13, no. 83, pp. 297-300, Feb. 1932.

[5] E. A. Ash and G. Nicholls, "Super-resolution Aperture Scanning Microscope," *Nature*, vol. 237, pp. 510-512, Jun. 1972.

[6] G. Binning, H. Rohrer, C. Gerber, and E. Weibel, "Surface Studies by Scanning Tunneling Microscopy," *Physical Review Letters*, vol. 45, no. 1, pp. 57-61, Jul. 1982.

[7] The Nobel Foundation. (1986) NobelPrize.org. [Online]. http://nobelprize.org/nobel_prizes/physics/laureates/1986/

[8] T. Yildirim. NIST Center for Neutron Research. [Online]. http://www.ncnr.nist.gov/staff/taner/nanotube/types.html

[9] G. Binning, C. F. Quate, and C. Gerber, "Atomic Force Microscope," *Physical Review Letters*, vol. 56, no. 9, pp. 930-933, Mar. 1986.

[10] Y. Martin, C. C. Williams, and H. K. Wickramasinghe, "Atomic force microscope-force mapping and profiling on a sub 100 angstrom scale," *Journal of Applied Physics*, vol. 61, no. 10, pp. 4723-4728, May 1987.

[11] G. Meyer and N. M. Amer, "Novel optical approach to atomic force microscopy," *Applied Physics Letters*, vol. 53, no. 12, pp. 1045-1047, Sep. 1988.

[12] Y. Martin, D. W. Abraham, and H. K. Wickramasinghe, "High-resolution capacitance measurement and potentiometry by force microscopy," *Appl. Phys. Lett.*, vol. 52, no. 13, pp. 1103-1105, Mar. 1988.

[13] J. E. Stern, B. D. Terris, H. J. Mamin, and D. Rugar, "Deposition and imaging of localized charge on insulator surfaces using a force microscope," *Applied Physics Letters*, vol. 53, no. 26, pp. 2717-2719, Dec. 1988.

[14] R. A. Said, M. Mittal, G. E. Bridges, and D. J. Thomson, "High frequency potential probe using electrostatic force microscopy," *Journal of Vacuum Science & Technology A*, vol. 12, no. 4, pp. 2591-2594, Aug. 1994.

[15] G. E. Bridges, R. A. Said, and D. J. Thomson, "Heterodyne electrostatic force microscopy for non-contact high frequency integrated circuit measurment," *Electronics Letters*, vol. 29, no. 16, pp. 1448-1449, Aug. 1993.

[16] D. Sarid, "Chapter 11: Electric Force Microscopy," in *Scanning force microscopy: with applications to electric, magnetic, and atomic forces*. New York: Oxford University Press, Inc., 1994, pp. 129-152.

[17] K. M. Cheng, Z. Weng, D. R. Oliver, D. J. Thomson, and G. E. Bridges, "Microelectromechanical Resonator Characterization Using Noncontact Parametric Electrostatic Excitation and Probing," *Journal of Microelectromechanical Systems*, vol. 16, no. 5, pp. 1054-1060, Oct. 2007.

[18] D. R. Oliver, A. Pu, D. J. Thomson, and G. E. Bridges, "Heterodyne electrostatic imaging of polarization due to a surface acoustic wave," *Applied Physics Letters*, vol. 79, no. 22, pp. 3729-3731, Sep. 2001.

[19] MikroMasch. [Online]. http://www.spmtips.com/tgz

[20] M. Chung, P. H. Cutler, T. E. Feuchtwang, and N. M. Miskovsky, "Solution of LaPlace's equation for a ridged conducting cone and planar counter-electrode: comparison with the solution to the Taylor conical model of a field emission LMIS+," *Journal De Physique*, vol. 45, no. 12, pp. C9145-C9152, Dec. 1984.

[21] S. Patil, A. V. Kulkarni, and C. V. Dharmdhikari, "Study of electrostatic force between a conducting tip in proximity with a metallic surface: Theory and experiment," *Journal of Applied Physics*, vol. 88, no. 11, pp. 6940-6942, Dec. 2000.

[22] B. D. Terris, J. E. Stern, D. Rugar, and H. J. Mamin, "Contact electrification using force microscopy," *Physical Review Letters*, vol. 63, no. 23, pp. 2669-2672, Dec. 1989.

[23] G. B. Jeffery, "On a form of the solution of Laplace's equation suitable for problems relating to two spheres," *Proc. R. Soc. Lond. A*, vol. 87, pp. 109-120, 1912.

[24] S. Belaidi, P. Girard, and G. Leveque, "Electrostatic forces acting on the tip in atomic force microscopy: Modelization and comparison with analytic expressions," *J. Appl. Phys.*, vol. 81, no. 3, pp. 1023-1030, Feb. 1997.

[25] S. Hudlet, M. Saint Jean, C. Guthmann, and J. Berger, "Evaluation of the capacitive force between an atomic force microscopy tip and a metallic surface," *Eur. Phys. J. B*, vol. 2, no. 1, pp. 5-10, Nov. 1997.

[26] C. Riedel, et al., "Determination of the nanoscale dielectric constant by means of a double pass method using electrostatic force microscopy," *Journal of Applied Physics*, vol. 106, no. 2, pp. 024315-024315-6, Jul. 2009.

[27] G. M. Sacha, E. Sahagun, and J. J. Saenz, "A method for calculating capacitances and electrostatic forces in atomic force microscopy," *Journal of Applied Physics*, vol. 101, no. 2, pp. 024310-024310-4, Jan. 2007.

[28] W. R. Smythe, *Static and Dynamic Electricity*. New York: McGraw-Hill, 1968.

[29] J. A. Stratton, *Electromagnetic Theory*. Piscataway: IEEE Press, 2007.

[30] J. D. Jackson, *Classical Electrodynamics 3rd Ed.* Hoboken: John Wiley & Sons, Inc., 1999.

[31] J. L. Hutter and J. Bechhoefer, "Calibration of atomic-force microscope tips," *Review of Scientific Instruments*, vol. 64, no. 7, pp. 1868-1873, Jul. 1993.

[32] MicroMasch. NSC18 Probe Datasheet. [Online]. http://www.spmtips.com/nsc/18/

[33] SRS Stanford Research Systems. (2006, Dec.) Model SR830 DSP Lock-In Amplifier User's Guide. [Online]. http://www.thinksrs.com/downloads/PDFs/Manuals/SR830m.pdf

[34] Micromasch. TGZ Series: Grating for Vertical Calibration. [Online]. http://www.spmtips.com/tgz

[35] D. Sarid, *Scanning Force Microscopy: With applications to Electric, Magnetic and Atomic Forces Revised Edition*. Oxford: Oxford University Press, 1994.

[36] E. Kreyszig, *Advanced Engineering Mathematics 10th Ed.* New York: John Wiley & Sons, Inc., 2011.

[37] G. Gramse, I. Casuso, J. Toset, L. Fumagalli, and G. Gomila, "Quantitative dielectric constant measurment of thin films by DC electrostatic force microscopy," *Nanotechnology*, vol. 20, pp. 1-8, Sep. 2009.

[38] G. Gomila, J. Toset, and L. Fumagalli, "Nanoscope capacitance microscopy of thin dielectric films," *Journal of Applied Physics*, vol. 104, no. 2, pp. 0243151-8, Jul. 2008.

[39] S. Gomez-Monivas, L. S. Froufe, R. Carminati, and J. J. Greffet, "Tip-shape effects on electrostatic force microscopy resolution," *Nanotechnology*, vol. 12, pp. 496-499, 2001.

[40] S. Gomez-Monivas, J. J. Saenz, R. Carminati, and J. J. Greffet, "Theory of electrostatic probe microscopy: A simple purturbative approach," *Applied Physics Letters*, vol. 76, no. 20, pp. 2955-2957, May 2000.

[41] P. P. Silvester and R. L. Ferrari, *Finite elements for electrical engineers 2nd Ed.* New York: Cambridge University Press, 1990.

[42] COMSOL Multiphysics, *COMSOL Multiphysics reference Guide v3.5a*. Los Angeles: COMSOL Multiphysics, 2008.